The FEBS Journal

FEBS PRESS science publishing by scientists

Tyrosine residues at the substrate binding site in human NQO1 homodimer: Protein conformational dynamics and optimization of substrate binding geometry

Maribel Rivero[1,2], Juan Luis Pacheco-Garcia[3], Pavla Vankova[4], Dmitry Loginov[5], Isabel Quereda-Moraleda[6], Jose Manuel Martin-Garcia[6], Petr Man[5], Angel Luis Pey[7,†] and Milagros Medina[1,2]

1 Department of Biochemistry and Molecular and Cellular Biology, Faculty of Sciences, University of Zaragoza, Zaragoza, Spain
2 Institute for Biocomputation and Physics of Complex Systems (BIFI), University of Zaragoza, Zaragoza, Spain
3 Department of Physical Chemistry, Faculty of Sciences, University of Granada, Granada, Spain
4 Institute of Biotechnology – BioCeV, Academy of Sciences of the Czech Republic, Vestec, Czech Republic
5 Institute of Microbiology – BioCeV, Academy of Sciences of the Czech Republic, Vestec, Czech Republic
6 Department of Crystallography and Structural Biology, Institute of Physical Chemistry Blas Cabrera, Spanish National Research Council (CSIC), Madrid, Spain
7 Department of Physical Chemistry, Unit of Excellence in Chemistry applied to Biomedicine and Environment and Institute of Biotechnology, University of Granada, Granada, Spain

Keywords
asymmetric kinetics; competent substrate binding; conformational dynamics; FAD; homodimeric enzyme; quinone oxidoreductase

Correspondence
M. Medina, Department of Biochemistry and Molecular and Cellular Biology, Faculty of Sciences, University of Zaragoza, 50009 Zaragoza, Spain
Tel: +34976762476
E-mail: mmedina@unizar.es

†Deceased. Dr. Ángel L. Pey sadly passed away before the completion of this work. This article is published in his memory.

(Received 20 October 2025, revised 19 January 2026, accepted 12 March 2026)

doi:10.1111/febs.70511

Human NQO1 is a homodimeric flavoenzyme essential for the redox metabolism of many substances and implicated in major global health challenges such as cancer and Alzheimer's disease. X-ray crystallographic studies have identified several residues within its substrate binding site (including Tyr126 and Tyr128) that may regulate catalytic competent binding of substrates, cofactor redox properties, half-site reactivity, and/or functional inter-active site negative cooperativity. To elucidate the functional role of Tyr126 and Tyr128, we generated point mutants at these positions and assessed their dynamics and kinetic properties. Hydrogen-deuterium exchange coupled to mass spectrometry revealed that non-conservative mutations, particularly at Tyr126, notably disrupted dynamics not only within the substrate binding site but also in structural elements connecting the two active sites of the NQO1 homodimer. Rapid-mixing pre-steady-state kinetics experiments of the reduction of NQO1 by NAD(P)H showed that mutations to Phe caused a mild decrease in hydride transfer (HT) efficiency from the coenzyme to the FAD cofactor. In contrast, mutations to Ala resulted in a significantly greater impact and mutations to Glu nearly abolished HT. Despite these effects, some mutations moderately affected the non-synchronous catalysis between the two alternating active sites, but hardly produced an impact on the selectivity for NADPH *versus* NADH as hydride donor coenzymes. However, all variants exhibited markedly impaired enzyme turnover, highlighting alterations in the enzyme's substrate specificity toward quinones. The data

Abbreviations
ASU, aymmetric unit; FAD, Flavin adenine dinucleotide; HDX-MS, Hydrogen-deuterium exchange monitored by mass spectrometry; HEPES, 2-[4-(2-hydroxyethyl)piperazin-1-yl]ethanesulfonic acid; HT, hydride transfer; K_{cat}, catalytic constant; K_d, dissociation constant; k_{HT}, HT rate constant; K_m, Michaelis–Menten constant; k_{obs}, observed rate constant; k_{prot}, second-order proteolysis rate constant; NAD^+, oxidized β-nicotinamide adenine dinucleotide; NADH, reduced β-nicotinamide adenine dinucleotide; NADPH, reduced nicotinamide adenine dinucleotide phosphate; NQO1, NAD(P)H:quinone oxidoreductase 1; ROS, reactive oxygen species; SDS/PAGE, Polyacrylamide gel electrophoresis in the presence of SDS; Tm, midpoint denaturation temperature; WT, wildtype.

presented here demonstrate that Tyr126 and Tyr128 optimize both substrate binding geometry as well as overall enzyme conformational dynamics during the asymmetric catalytic cycle of the NQO1 homodimer.

Introduction

The NAD(P)H:quinone oxidoreductase 1 (NQO1; UniProt ID P15559) flavoenzyme plays a pivotal role in cellular defense mechanisms against oxidative stress and toxic quinones, contributing to the control of cellular redox homeostasis. It is a two-electron reductase that utilizes NADH or NADPH as hydride donors to catalyze the reduction of quinones to hydroquinones [1,2]. This reaction is essential for detoxification, as it prevents the formation of reactive oxygen species (ROS) through redox cycling. NQO1 is expressed in multiple tissues, and its expression is regulated by several pathways, primarily through the antioxidant response element mediated by the transcription factor NRF2 [1,2]. Its physiological functions extend beyond being an enzyme, since it also stabilizes key regulatory proteins such as p53, p73, and HIF1α [1,3]. Additionally, NQO1 has garnered significant interest in cancer research due to its overexpression in certain tumors, making it a potential therapeutic target [4].

Structurally, NQO1 is a homodimer in which each monomer binds one flavin adenine dinucleotide (FAD) molecule as cofactor, making two active sites located at the monomer-monomer interface. Each active site can accommodate the hydride donors NADH or NADPH, as well as the hydride acceptor quinones [2,4]. Residues from both monomers contribute to each of the two, nominally identical, active sites in NQO1 (Fig. 1A). This arrangement promotes the two-electron reduction through hydride transfer (HT), leading to the reduction of quinones to hydroquinones [5,6]. This mechanism prevents redox cycling and minimizes oxidative stress in contrast to one-electron reduction that generates ROS. Notably, pre-steady-state enzyme kinetic analysis of the human NQO1 (hereafter NQO1) reaction revealed the existence of two different pathways for the FAD HT processes during both the flavin reductive and oxidative half-reactions. These findings indicate that the reduction and oxidation of the two FAD cofactors within the NQO1 homodimer occur at different rates, supporting the existence of functional negative cooperativity [7,8]. Furthermore, room temperature crystallographic structures along with molecular dynamics simulations for the interaction of NQO1 with NADH indicate that one of the two active sites within the homodimer preferentially holds the coenzyme in a catalytically competent conformation over the other [6]. This asymmetry further explains cooperative effects observed in the binding of FAD, NADH, and inhibitors [9–12].

Elucidating the structural dynamics, catalytic mechanism, and regulatory features of NQO1 is essential for understanding its roles in health and disease [4], as well as for developing more effective and structure-based inhibitors for cancer therapies [13]. Structural studies have identified a set of residues that collectively orchestrate the NQO1 catalysis. Among them, Tyr126 and Tyr128 (numbered excluding Met1) are proposed to play critical roles in stabilizing substrates and catalytic intermediates throughout the oxidation–reduction process [5,6]. These residues are thought to participate in hydrogen bonding and stacking interactions with the substrates (Fig. 1B), guiding their optimal positioning within the active site for catalysis [13]. Moreover, a recent study has also shown that Tyr126 and Tyr128 may have been evolutionarily selected to confer specificity toward NADH and NADPH coenzymes, a distinctive feature that differentiates NQO1 from its paralog quinone oxidoreductase 2 (NQO2), which displays very low efficiency with either coenzyme [14].

In this work, we conducted an in-depth experimental investigation of the roles of Tyr126 and Tyr128 in the conformational stability and function of NQO1. These residues were conservatively mutated to Phe and non-conservatively to Ala, while substitutions to Glu were introduced to probe electrostatics at the substrate binding site. Mutations to Phe and Ala noticeably affected NQO1 catalytic activity, whereas the mutations to Glu nearly abolished it. Furthermore, mutations altered the native NQO1 local flexibility, both in the absence and presence of the coenzyme. These results indicate that Tyr126 and Tyr128 residues are essential for maintaining the conformational dynamics to ensure correct positioning of the substrates for efficient catalysis.

Results and discussion

The rationale for generating mutants at Tyr126 and Tyr128

Several mutants were produced at positions of Tyr126 and Tyr128 at the substrate binding site of NQO1

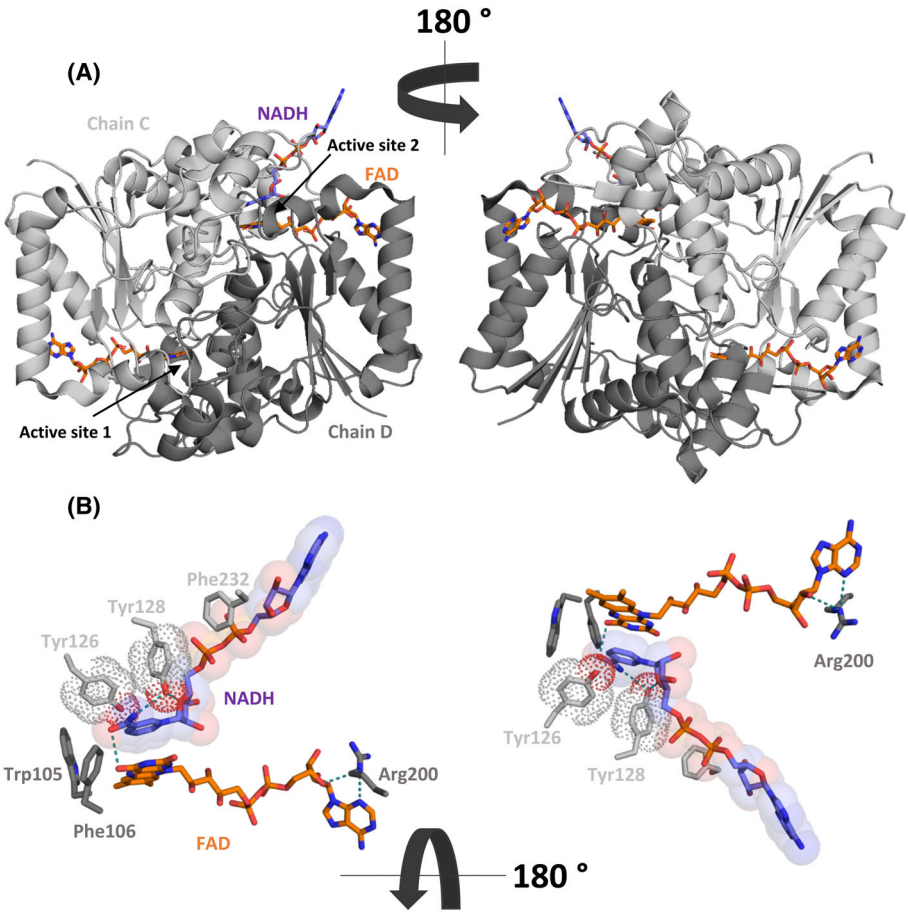

Fig. 1. Crystal Structure of NQO1 and structural arrangement of Tyr126 and Tyr128 relative to NAD^+/H and FAD. (A) Crystal structure of the NQO1 homodimer in complex with NAD^+/H (PDB 8RFM, chains C and D in ASU). The two NQO1 protomers are shown as light and dark gray cartoon, with the FAD cofactors and the NAD^+/H coenzyme (in active site 2) displayed as sticks, with carbon atoms colored in orange and violet, respectively. (B) Close-up view of main interactions and key residues at the FAD and NAD^+/H binding sites. Key residues (numbered excluding Met1) at the active site and interacting with the non-reactive moieties of FAD and NAD^+/H are shown as sticks. The image illustrates the stacking of the nicotinamide against the isoalloxazine of FAD, as well as hydrogen bonds (steel lines) formed between the hydroxyl group of Tyr128 and atoms of the nicotinamide nucleotide of NADH, the side-chain of Arg200 and the adenine nucleotide of FAD, and the amide of the NADH's nicotinamide and the isoalloxazine of FAD. The Van der Waals surfaces of the Tyr126 and Tyr128 side-chains are represented as dotted spheres, while those for the coenzyme atoms are shown as transparent spheres. Structure visualized using PYMOL Software.

(Figs 1 and S1). Two mutations were quite conservative (Tyr126Phe and Tyr128Phe), whereas four were much more disruptive, almost fully removing the bulky side-chain (Tyr126Ala and Tyr128Ala) or introducing a negative charge with changes in side-chain size and volume (Tyr126Glu and Tyr128Glu).

All NQO1 variants were produced at good yields and isolated to a high purity (Fig. S2). As purified, all of them showed the typical visible spectra for an almost saturated form of NQO1 with FAD, except for the variant Tyr126Ala that hardly showed 30% FAD occupancy (Fig. S3A). NQO1 variants exhibited a minor alteration in thermal stability compared to the wild-type (WT) enzyme. Specifically, Tyr126Ala and Tyr126Glu showed a slight decrease in T_m (around 2.5–3 °C), while the other variants showed very minor increases in midpoint denaturation temperature (T_m) (Fig. 2A). Given that FAD binding is associated with the thermal stability of NQO1 [11], the reduced stability observed in Tyr126Ala may agree with a lower affinity for FAD, consistent with our visible absorption measurements (Fig. S3B). Interestingly, when incubated with increasing concentrations of NAD^+, the thermal stability of the WT and Tyr128 mutants remained largely unchanged (Fig. 2B,C). These results show that coenzyme binding does not

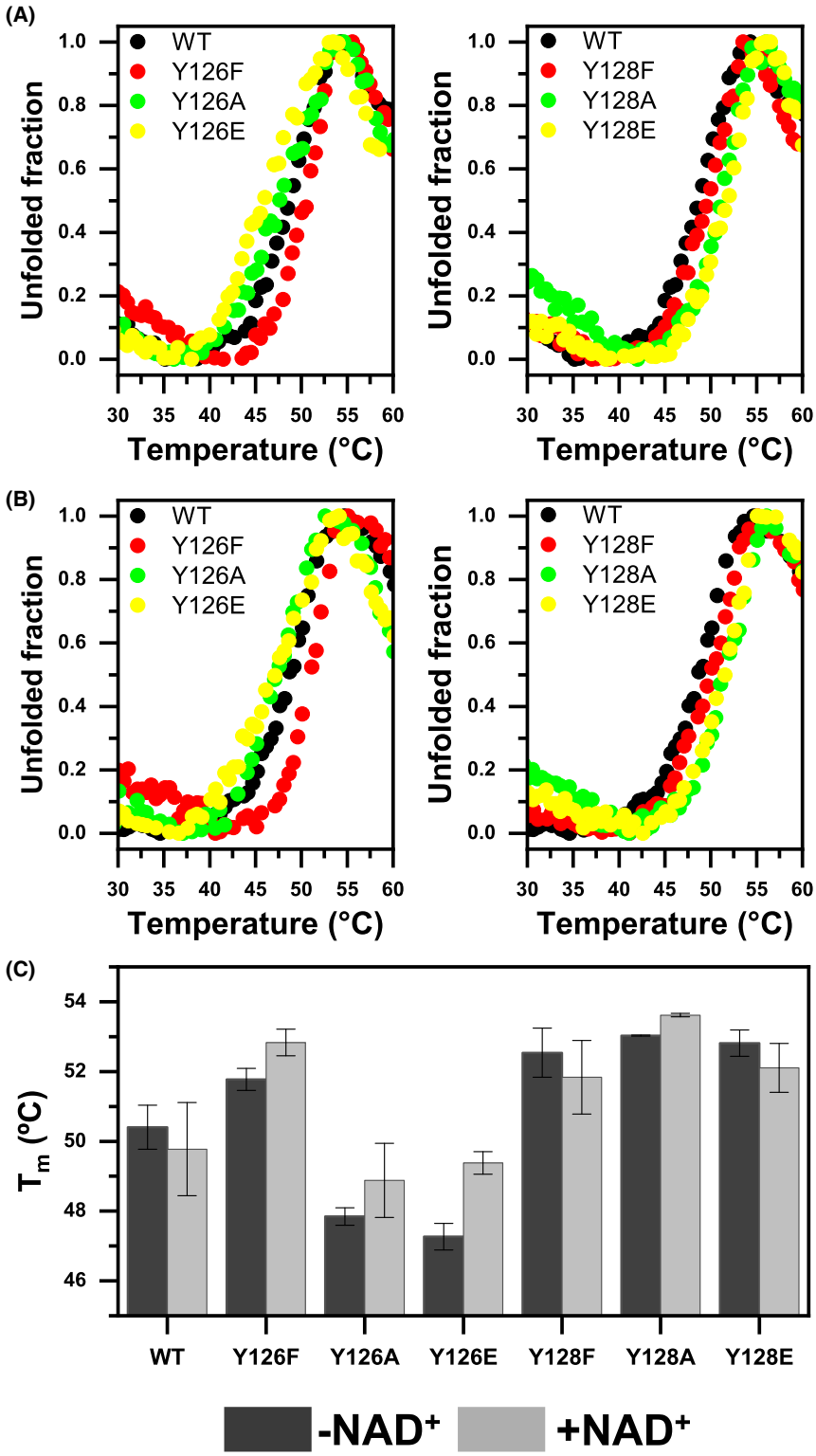

Fig. 2. Thermal denaturation of NQO1 variants. Normalized thermal denaturation profiles as followed by Trp fluorescence emission for NQO1 variants in the (A) absence and (B) presence of NAD^+. Data for a single representative experiment for each variant are shown for the sake of clarity. (C) T_m values determined for thermal denaturation of NQO1 variants in the absence (dark gray) and the presence of NAD^+ (light gray) (mean ± s.d., $n = 3$).

enhance NQO1 thermal stability of neither the WT nor the variants, preventing a definitive conclusion whether the mutations impair binding. However, the coenzyme produced a very mild stabilizing effect in the less stable Tyr126Ala and Tyr126Glu mutants, suggesting that at least these variants may retain some ability to interact with NAD^+.

Mutations of Tyr126 and Tyr128 modulate the conformational stability of NQO1

Hydrogen-deuterium exchange mass spectrometry (HDX-MS) has been instrumental in quantifying the effect of mutations and ligand binding on the local structural stability and function of NQO1 [8,15–17]. The HDX behavior of WT NQO1 essentially followed an EX2 mechanism in which the observed exchange rate constants reflect in part the thermodynamic and conformational stability of the exchanging local regions or segments [15]. In most cases, the exchanging transients were well described by a single-exponential function typically with a significant burst phase (Figs S4, S5, S6, S7 and S8 and Table S1). This indicates significant conformational diversity in the native-state ensemble of WT NQO1 (FAD-bound NQO1), likely associated with its cooperative functional behavior toward substrates and inhibitors [7,11,15,18].

Here, we first used HDX-MS to quantify the impact of mutations at Tyr126 and Tyr128 on the local conformational stability of NQO1 (when saturated with FAD). The most remarkable effects were found in the Tyr126Ala and Tyr126Glu variants, while the behavior of Tyr126Phe and Tyr128Phe was WT-like (Figs 3A and 4A,B). In Tyr126Ala and Tyr126Glu variants, the compactness of regions 42–90, 105–112, 119–124, 129–141, 231–240 and 262–273 was thermodynamically reduced (according to an EX2 mechanism [15]), particularly of segments 54–74 and 131–140. Destabilization of the N-terminal segment 54–74 was further confirmed by proteolysis experiments with thermolysin that cleaves between residues 71–72 [19], and showed a remarkable local thermodynamic destabilization of this region by the mutations Tyr126Ala and Tyr126Glu (~1.4–1.6 $kcal{\cdot}mol^{-1}$), whereas the mutant Tyr128Ala exhibited a milder local destabilization (~0.5 $kcal{\cdot}mol^{-1}$) (Figs 5 and S9, Table S2). In general, these locally destabilized segments are not directly involved in the NQO1 active site, but when mapped on NQO1 structure they surround the substrate binding site with the two tyrosine residues forming the core of the ring (Fig. 3B). The only exception is the 105–112 segment, which contains strongly conserved residues, some of them, as Trp105 and Phe106, contributing from the other protomer, being critical for forming the isoalloxazine active site and playing a vital role in catalysis [19]. Of note is that the destabilization induced by Tyr126Ala and Tyr126Glu mutations propagates from the mutation site toward regions 42–90 in both protomers (Figs 3B and 4A,B). These regions face each other and serve as a long-range connection between the two substrate binding sites within the homodimer.

On the contrary, the Tyr128Glu replacement slightly stabilizes some of the above-mentioned regions relative to WT NQO1 (blue instead of red in Figs 3A and 4A,B), while the rest of mutations produced minimal effects on the local and long-range conformational stability of NQO1 (Figs 3A and 4A,B and Table S2). The differing HDX effects of Ala and Glu mutations at Tyr126 and Tyr128 can be a consequence of the distinct interactions that these side-chains make with the protein environment and the coenzyme (Fig. 1). The side-chain of Tyr128 makes minimal contacts with other protein residues, contributing to the channel that guides the nicotinamide of NADH to the active site and directly hydrogen bonding its hydroxyl to the nicotinamide and ribose moiety of NAD^+/H [6]. In contrast, Tyr126 is deeply embedded at the bottom of the active site cavity, which likely enhances its significance in NQO1 conformational dynamics and function. Tyr126 contacts the main chain atoms of the 123–126 loop as well as the Phe178 side-chain; meanwhile, its hydroxyl directly points to the nicotinamide of the bound coenzyme. Furthermore, former molecular dynamics simulations indicated that the transient stacking interaction of the nicotinamide is more prevalent to Tyr126 than to Tyr128 and envisaged short-lived polar contacts between the Tyr126 hydroxyl group and the amide atoms of the coenzyme [6].

NAD^+ binding reduces the conformational flexibility of WT NQO1, but has a reduced effect on Tyr to Ala/Glu mutants

We also analyzed the effects of binding of NAD^+ to NQO1 on its conformational stability and flexibility by HDX-MS (Figs 6A and 7, and Table S1). In the presence of a large excess of NAD^+, the WT protein showed moderate conformational stabilization (between 10 and 20 $\Delta\%D_{av}$, Tables S3 and S4) of three main segments, 65–75, 132–140, and 232–239. Using a cut-off of 5–10 $\Delta\%D_{av}$, segments 42–64, 76–89, 121–124, 129–131, 141, 191–201, 229–231, 240–244, and 269–270 were also mildly stabilized (Figs 6B and 7 and Table S1). Notably, these

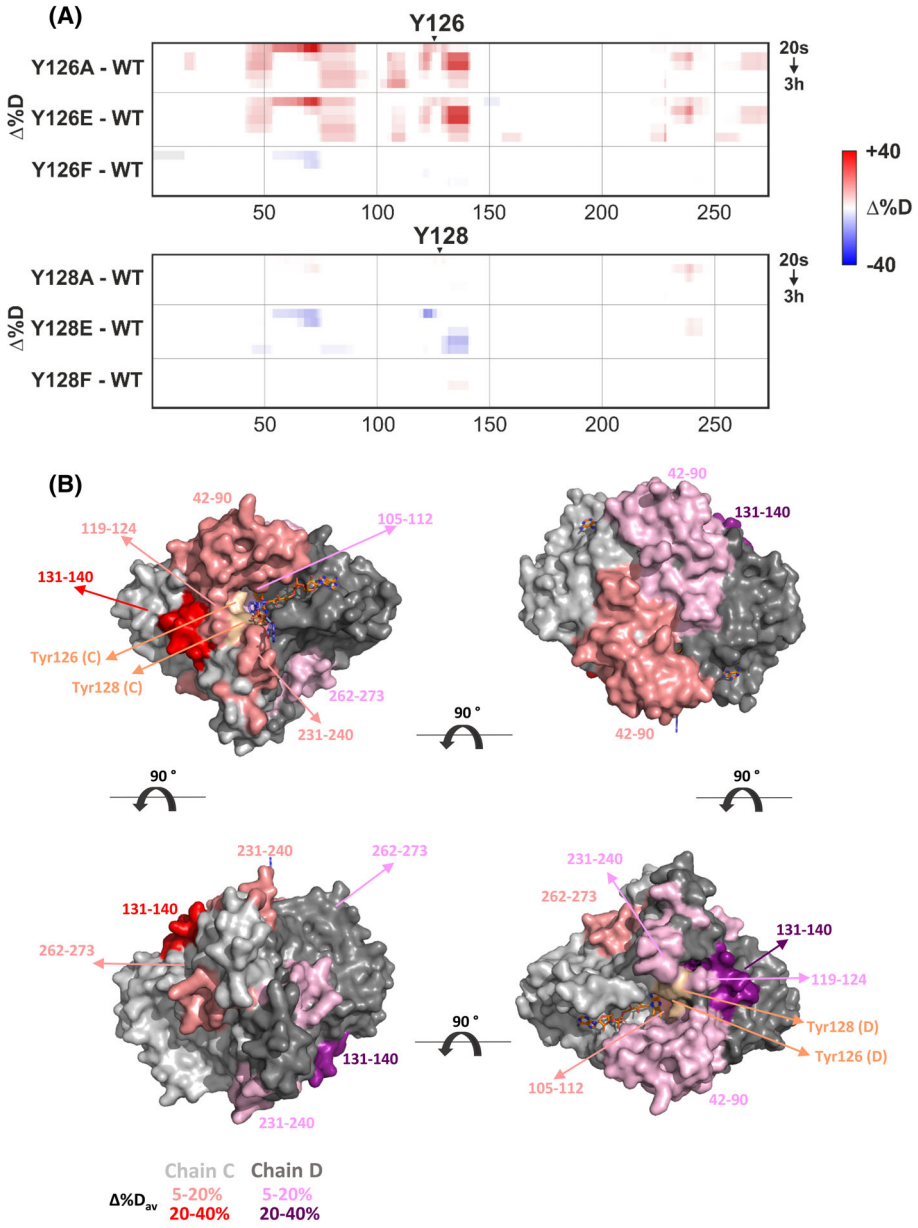

Fig. 3. Effects of Tyr126 and Tyr128 variants on the HDX-MS of NQO1. (A) Differential HDX-MS heat maps between mutants and WT for NQO1 (with excess of FAD) showing regions of conformational destabilization (red shades) or protection (blue shades) (Δ%D) induced by mutations of Tyr126 (upper panel) and Tyr128 (lower panel). The x-axis indicates the NQO1 sequence, while different rows for each mutant correspond to exchange times of 20 s, 3 min, 10 min, 1 h, and 3 h. The color scale is shown to the right. (B) Mapping of regions destabilized by the Tyr126Ala and Tyr126Glu mutations on the 3D structure of the NQO1:NAD$^+$/H homodimer (PDB 8RFM). Each NQO1 protomer (chains C and D in the ASU) is shown as a light and dark gray surface. The FAD cofactors and the NAD$^+$/H coenzyme are shown as sticks with carbons in orange and violet, respectively. Mild and moderate destabilized regions are respectively highlighted in dark and pale reds for protomer C and dark and pale purples for protomer D. Residues 126 and 128 are highlighted in wheat. The figure shows for each mutant a side view at the binding site occupied by the NAD$^+$/H coenzyme in PDB 8RFM as well as subsequent x-axis 90° rotations from the initial view. Heat mapping of Δ%D$_{av}$ data for each individual mutant regarding the WT NQO1 can be found in Fig. 4. Structure visualized using PYMOL Software.

NAD$^+$-induced changes not only affected the coenzyme binding site locally but also propagated over long ranges (Figs 6A, 7 and S10), inducing a global conformational stiffening that can be associated with reduced plasticity, consistent with the decreased flexibility observed in the crystallographic structure of the

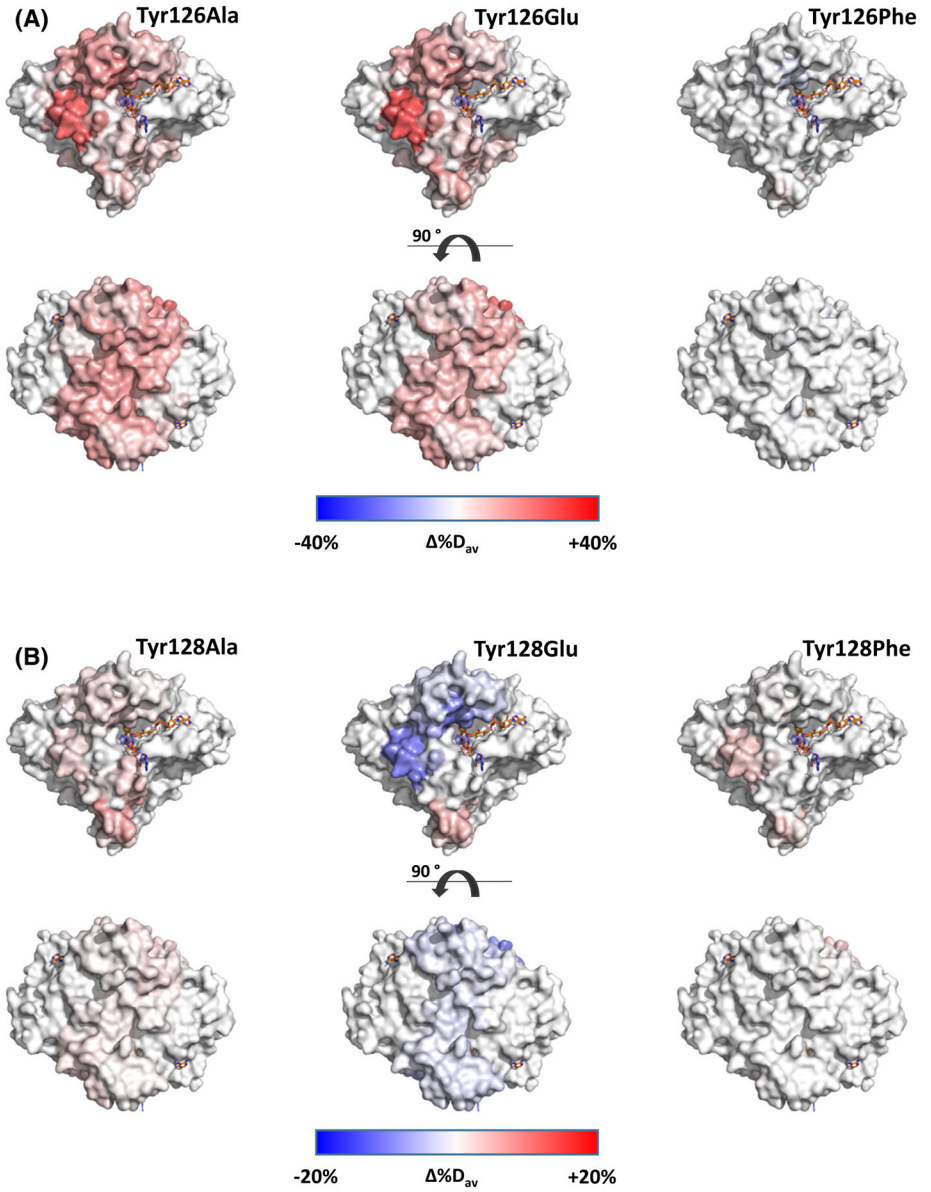

Fig. 4. Effects of Tyr126 and Tyr128 mutations on NQO1 conformational stability. Heat mapping of HDX-MS Δ%D_{av} data (Tables S3 and S4) for the difference between each mutant and WT NQO1, with excess of FAD (data from Fig. 3A), on the 3D structure of the NQO1:NAD^+/H homodimer (PDB 8RFM, chains C and D) for mutants at position (A) 126 and (B) 128. For each mutant, plots highlight segments exhibiting destabilization (red shades) and protection (blue shades) compared to the equivalent segments in WT NQO1. The FAD cofactors and the NAD^+/H coenzyme are indicated as sticks with carbons in orange and violet, respectively. The figure shows a side view of the binding site occupied by the NAD^+/H coenzyme in PDB 8RFM (top panels) as well as an x-axis 90° rotation of that view (bottom panels) for all variants. Structure visualized using PYMOL Software.

NQO1:NAD^+/H complex upon coenzyme binding [6]. Furthermore, comparison of Figs 3B and 7 clearly illustrates that NAD^+ binding particularly stabilizes regions of the WT enzyme that match to regions slightly destabilized in Tyr128Ala but particularly destabilized in Tyr126Ala/Glu mutants. This suggests that these regions are part of the global conformational network essential for productive coenzyme binding and that such regions are particularly destabilized by the indicated mutations.

We then compared the ability of NAD^+ to stabilize each mutant relative to the stabilization observed in WT NQO1. Mutants Tyr128Phe and, particularly, Tyr126Phe showed a stabilizing effect similar to that

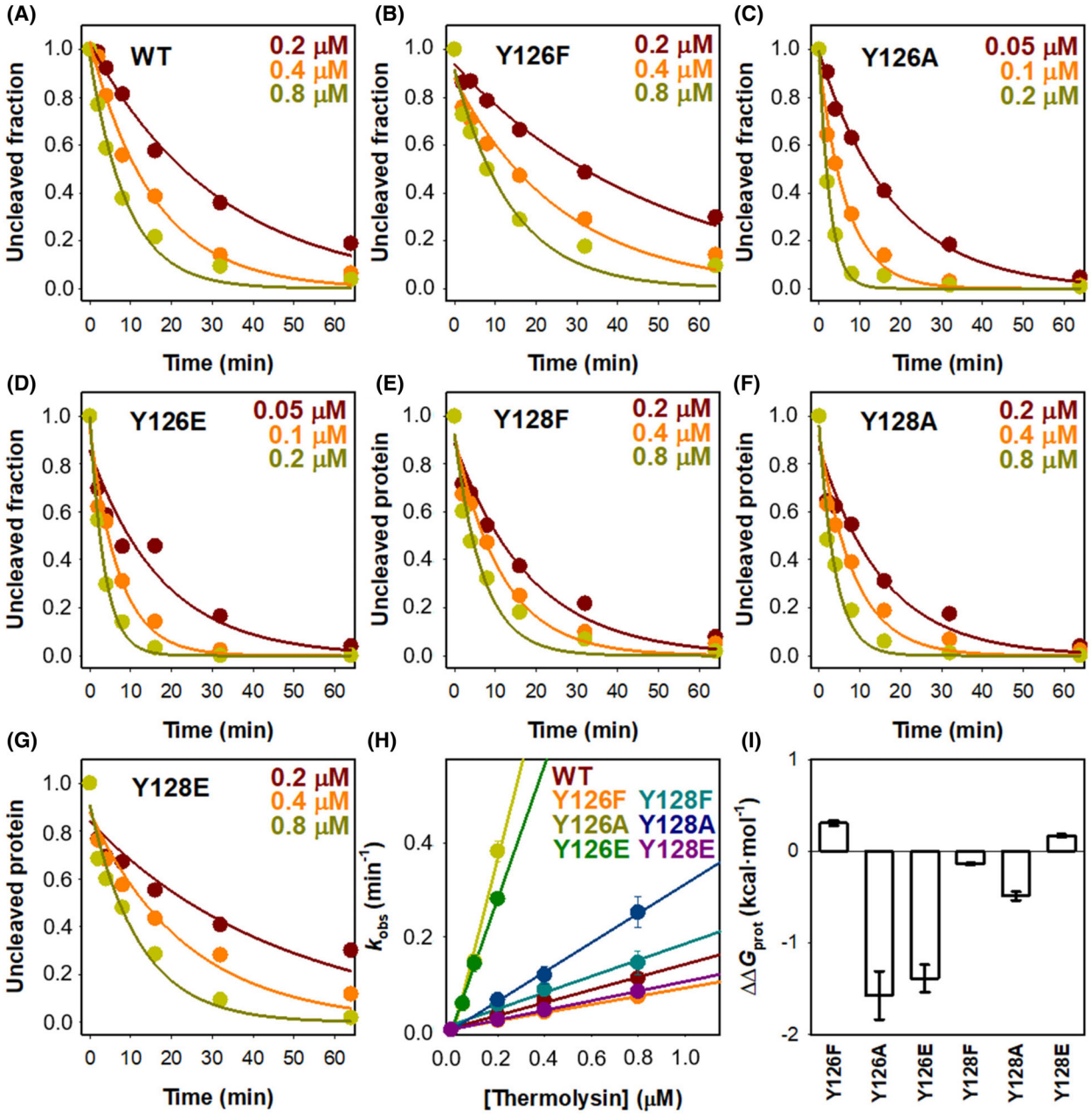

Fig. 5. Proteolysis kinetics of NQO1 variants in the presence of thermolysin. (A–G) Densitometry analysis of SDS/PAGE gels for each NQO1 variant incubated with increasing concentrations of thermolysin (color code indicated in each panel; data from a single experiment). Lines represent best-fits to a single-exponential function that yield the first-order rate constants (k_{obs}). (H) Dependence of k_{obs} on thermolysin concentration. Colors denote the NQO1 variants analyzed, and errors correspond to the fits shown in panels A-G. Lines represent best-fits to a linear function whose slopes provide the second-order rate constants k_{prot} (Table S2). (I) Effect of mutations on the local conformational thermodynamic stability in the vicinity of the primary cleavage site (S71-V72; [20]) from the values of k_{prot} as follows: $\Delta\Delta G_{prot} = -RT\ln(k_{prot(mutant)}/(k_{prot(WT)})$.

observed for the WT (neutral $\Delta\%D_{av}$ values across their sequences and structures) (Figs 8A,B and 9, Tables S3 and S4). NAD^+ has hardly any stabilizing effect on segments destabilized by the Tyr126Ala and Tyr126Glu mutations, while it has a mild effect on Tyr128Ala mutation (compare red shaded segments in Figs 4A and 9A). In the case of the Tyr128Glu mutant, despite the data suggesting over-stabilization relative to

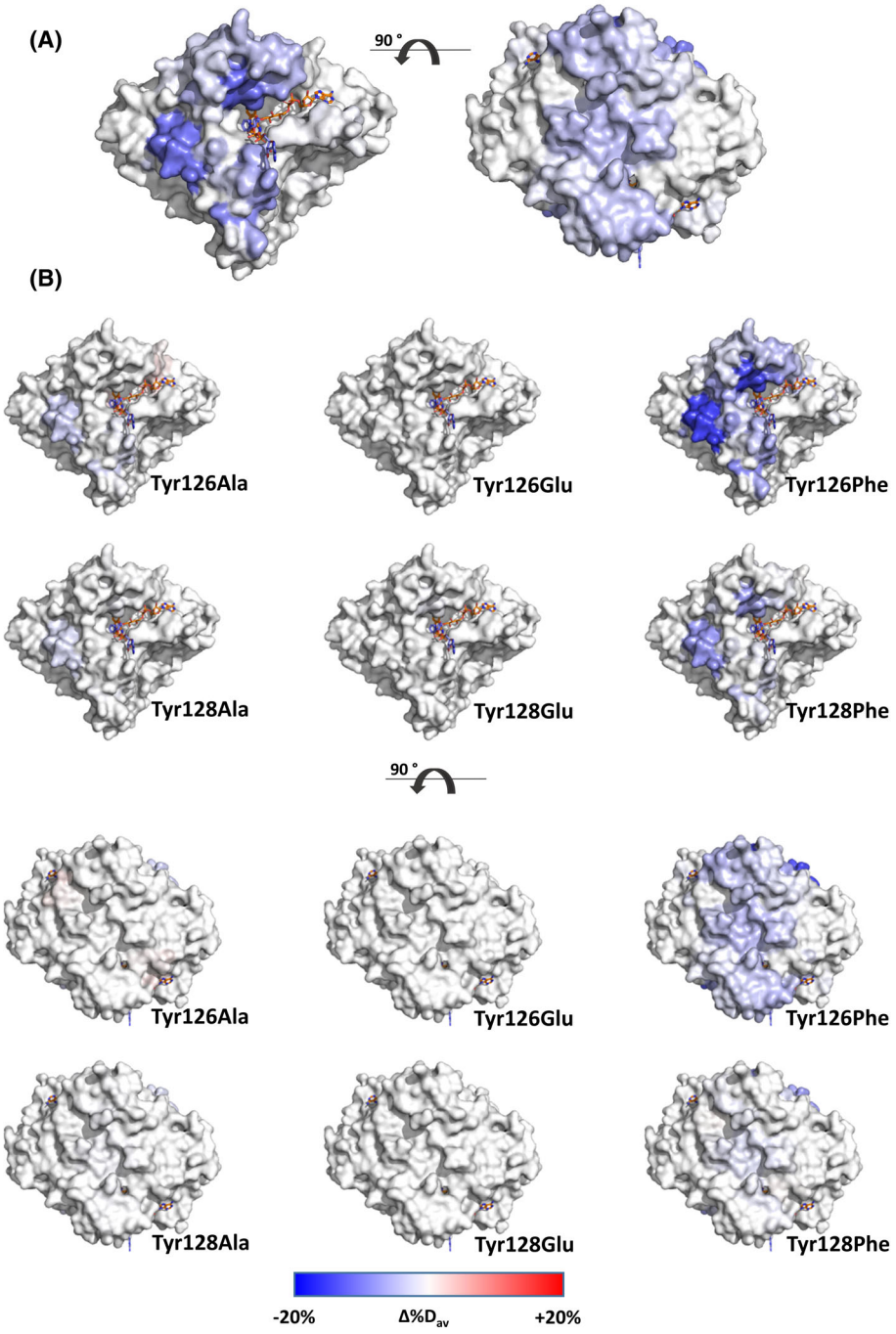

Fig. 6. Conformational stabilization of NQO1 variants by NAD^+. Heat mapping on the 3D structure of the NQO1:NAD^+/H homodimer (PDB 8RFM, chains C and D) of HDX-MS $\Delta\%D_{av}$ data showing segments stabilized by the presence of NAD^+. (A) Mapping of data for WT NQO1. The figure shows a side view of the binding site occupied by the NAD^+/H coenzyme in PDB 8RFM (left) as well as an x-axis 90° rotation of that view (right). (B) Mapping of data for the Tyr126 and Tyr128 mutants. The figure shows a side view of the binding site occupied by the NAD^+/H coenzyme in PDB 8RFM (top panels) as well as an x-axis 90° rotation of that view (bottom panels) for each variant. The FAD cofactors and the NAD^+/H coenzyme are indicated as sticks with carbons in orange and violet, respectively. Structure visualized using PYMOL Software.

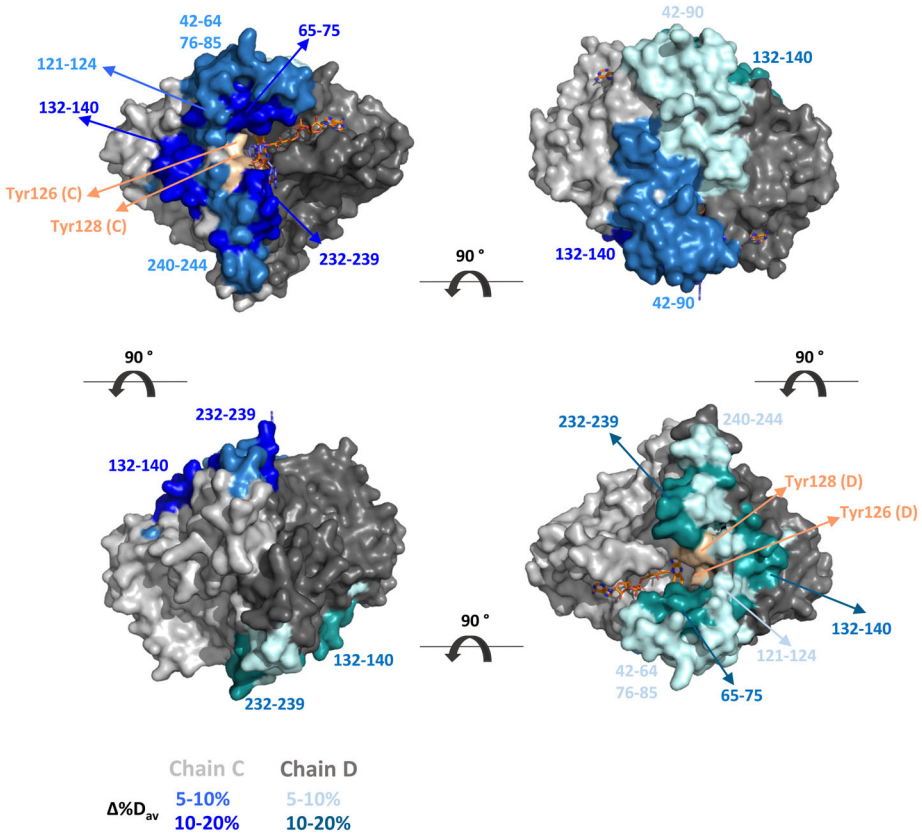

Fig. 7. Global stabilization of WT NQO1 upon binding of NAD^+. Mapping of regions stabilized upon NAD^+ binding on the 3D structure of the NQO1:NAD^+/H homodimer (PDB 8RFM). Each NQO1 protomer (chains C and D in the ASU) is shown as a light and dark gray surface. The FAD cofactors and the NAD^+/H coenzyme are depicted as sticks with the carbons in orange and violet, respectively. Mild and moderate stabilized regions are respectively highlighted in dark and pale blues for protomer C and dark and pale greens for protomer D. Residues 126 and 128 are highlighted in wheat. The figure shows for each mutant a side view at the binding site occupied by the NAD^+/H coenzyme in PDB 8RFM as well as subsequent x-axis 90° rotations from the initial view. Heat mapping of $\Delta\%D_{av}$ data can be found in Fig. 6 and D_{av} values for all segments are provided in Tables S3 and S4. Structure visualized using PYMOL Software.

WT NQO1:NAD^+ (Figs 8A and 9B), it is worth reminding that this mutation induces a protein conformational stiffening (Figs 3A and 4B) that, apparently, is stronger than the one induced by the coenzyme in the WT enzyme. These observations support altered NAD^+ binding by mutations to Ala and Glu (possibly due to altered affinity). In agreement, comparing the pattern for deuterium incorporation for WT and the mutants (Figs 6A,B and 8B), both glutamate variants failed to show any stabilization when NAD^+ was added to the exchange reaction while Phe variants show the closest to WT levels of stabilization and Ala variants only show some minor stabilization. Consequently, when in the presence of NAD^+, the mutants Tyr128Ala and, particularly, Tyr126Ala/Glu are less compact than the WT protein at these segments (Figs 6 and 9). In the Tyr126Ala/Glu variants, this is further supported by increased conformational flexibility, which propagates far from the mutation sites and connects both active sites through the same protomer–protomer interface that links them upon WT NQO1 stabilization by NAD^+ (Figs 3A, 7 and 9A).

Tyr126 and Tyr128 are key players for the efficient catalytic activity of NQO1

Pre-steady-state enzyme kinetic analysis of WT NQO1 has revealed two different pathways for the FAD reductive half-reaction by the NADH coenzyme, termed *fast* and *slow*, indicating that the reduction of the two FAD molecules within the NQO1 homodimer occurs at different rates in a non-synchronized manner [7]. Moreover, only the *fast* process was compatible with the catalytic constant, making the flavin reductive half-reaction the limiting step in overall catalysis under steady-state conditions, and indicating that the *slow*

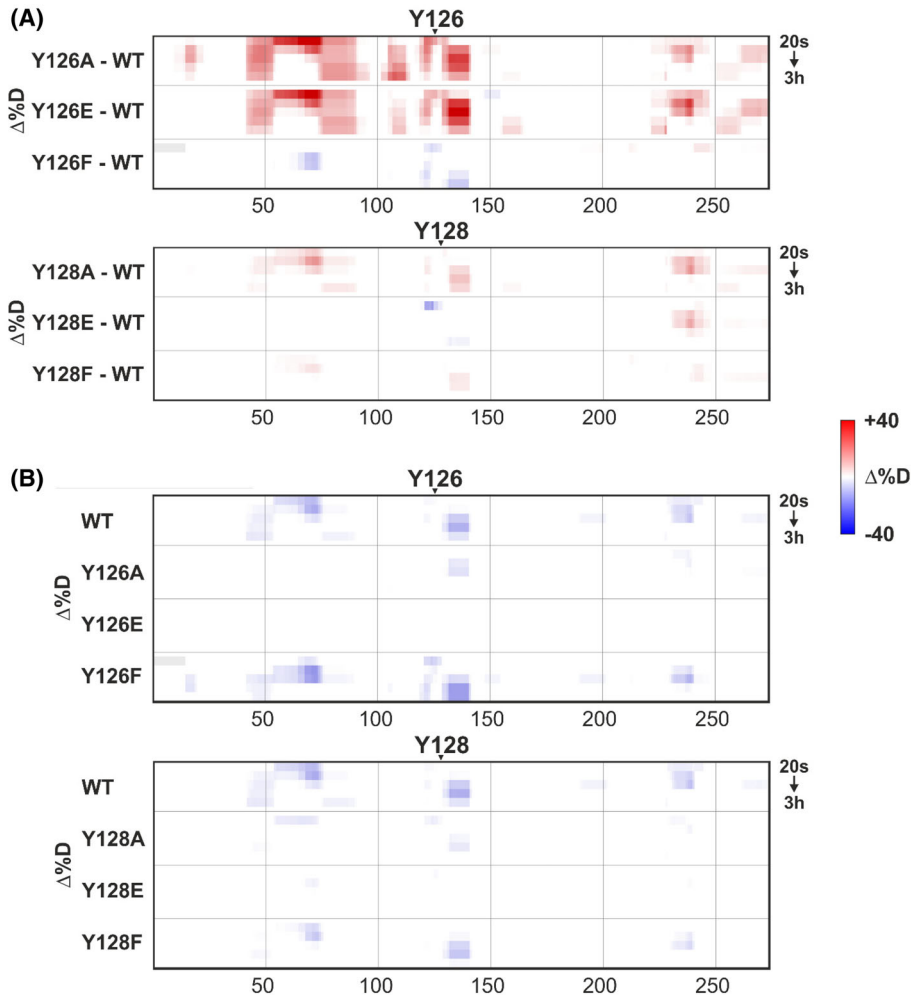

Fig. 8. Effects of the binding of NAD^+ on the HDX-MS profiles of NQO1 variants. Differential HDX-MS heat maps for WT NQO1 and Tyr126/Tyr128 variants in the presence of NAD^+. (A) Absence (red shades) or presence (blue shades) of conformational stabilization (Δ%D) relative to the corresponding WT NQO1 segments caused by mutations at Tyr126 (upper panel) and Tyr128 (lower panel) both in the presence of NAD^+ (with excess of FAD and NAD^+). (B) Differences in deuterium incorporation for each NQO1 variant when in the presence and absence of NAD^+. The x-axis represents the NQO1 sequence; exchange reaction times for each row are indicated on the right, and the color scale is shown to the right of the plots.

phase possibly represents an off-pathway process that is catalytically irrelevant [7]. Such behavior has also been found in most point mutants so far evaluated [8,17,19]. When evaluating the NADH-dependent flavin reductive half-reaction for variants at Tyr126 and Tyr128, mutants specifically perturbed some features compared to the WT (Table 1 and Fig. 10). Mutations affected times required for achieving reduction of each of the two FAD cofactors within the homodimer and/or ratio of oxidized/reduced FAD cofactors upon achieving the reaction equilibrium (Figs 10 and 11). Nonetheless, spectral deconvolution of multi-wavelength time-resolved data indicated that for all variants reduction of the two FAD cofactors occurs through two kinetically separated processes, as previously described for the WT enzyme [7] (Fig. 11). Noticeably, the deleterious effects caused by some of the mutations in the $k_{obs,fast}$ values (see Fig. 12A–D and Table 1) enabled experimental observation of the FAD reductive half-reaction using NADPH as hydride donor at different coenzyme concentrations, a process that was too fast to be captured in the WT enzyme and earlier studied variants (Figs S11 and S12) [7].

The variants Tyr126Ala or Tyr128Ala became nearly fully reduced by both NADH and NADPH (Figs 10A,B, S11A and S11B). Moreover, time-dependent spectral deconvolution revealed that in both variants the FAD reduction process exhibited

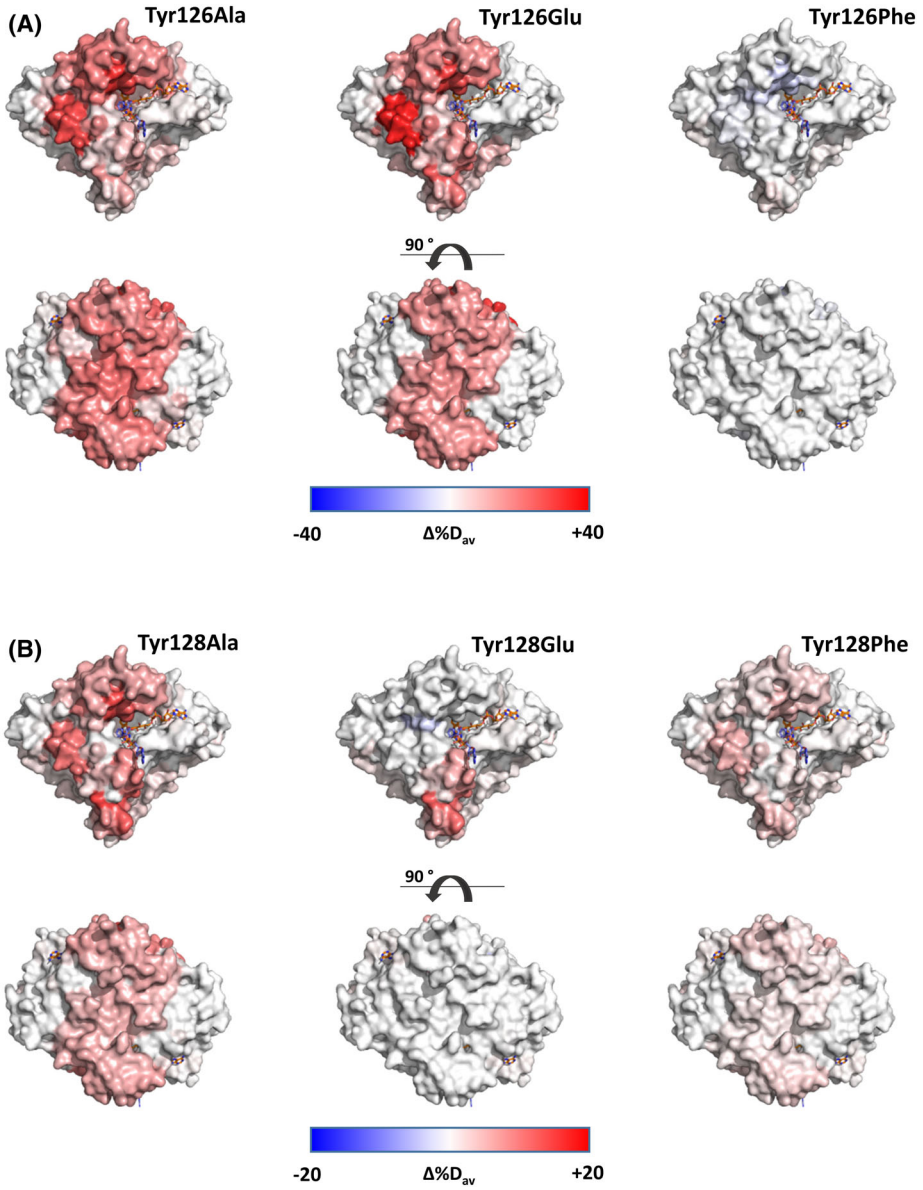

Fig. 9. Effects of Tyr126 and Tyr128 mutations on NQO1 conformational stability upon binding of NAD^+. Mapping of HDX-MS $\Delta\%D_{av}$ data for the difference between each mutant and WT NQO1, both with excess of NAD^+ (data from Fig. 8A), on the 3D structure of the NQO1: NAD^+/H homodimer (PDB 8RFM, chains C and D) for mutants at position (A) 126 and (B) 128. Plots highlight segments for each one of the mutants exhibiting absence of stabilization (red shades) and over-stabilization (blue shades) when in the presence of the coenzyme regarding the equivalent segments in WT NQO1-NAD^+ samples. The FAD cofactors and the NAD^+/H coenzyme are shown as sticks with carbons in orange and violet, respectively. The figure shows for each mutant a side view at the binding site occupied by the NAD^+/H coenzyme in PDB 8RFM (top) as well as a x-axis 90° rotation of that view (bottom). Structure visualized using PYMOL Software.

distinct *fast* and *slow* processes, resembling the kinetic behavior observed in WT enzyme [7,19], with the *fast* phase showing just a slightly larger amplitude (representative analyses are shown in Figs 11A,B, S12A and S12B). Nonetheless, these mutations had a particularly negative impact on $k_{obs,fast}$ values (the observed rate constant for the *fast* process) across the range of NAD(P)H concentration evaluated, while $k_{obs,slow}$ values generally remained closer to those of the WT enzyme (Figs 12A–D and Table 1). As observed for the reduction of the WT enzyme by NADH, the $k_{obs,fast}$ values of Tyr126Ala and Tyr128Ala showed a hyperbolic dependence on both NADH and NADPH coenzyme concentrations (Fig. 12A,C). This allowed

Table 1. Tyr126 and Tyr128 with NAD(P)H. Primary data and fittings are shown in Figs 12A to 12D.

NQO1 Reduction by NADH

	Fast			Slow		
	k_{HT} (s^{-1})	K_d^{NADH} (μM)	k_{HT}/K_d^{NADH} ($s^{-1}\cdot\mu M^{-1}$)	k_{HT} (s^{-1})	K_d^{NADH} (μM)	k_{HT}/K_d^{NADH} ($s^{-1}\cdot\mu M^{-1}$)
WT[a]	281 ± 12	15.2 ± 1.9	18.5 ± 2.4	14.3 ± 1.5	8.2 ± 3.3	1.7 ± 0.7
Tyr126Ala	50 ± 2	32 ± 2	1.7 ± 0.3	24 ± 2	45 ± 10	$5.3 \pm 1.5 \cdot 10^{-1}$
Tyr128Ala	53 ± 1	19 ± 1	2.8 ± 0.2	9.3 ± 0.8	10.4 ± 4.4	$8.9 \pm 4.5 \cdot 10^{-1}$
Tyr126Glu	$1.8 \pm 0.4 \cdot 10^{-1}$[b]	N.a.[b]	N.a.[b]	$2.8 \pm 1.4 \cdot 10^{-2}$[b]	N.a.[b]	N.a.[b]
Tyr128Glu	$9.7 \pm 0.8 \cdot 10^{-2}$[c]	N.a.[c]	N.a.[c]	$3.9 \pm 0.2 \cdot 10^{-2}$[c]	N.a.[c]	N.a.[c]
Tyr126Phe	290 ± 12	28 ± 3	10.3 ± 1.5	16.1 ± 1.5	33 ± 5	$4.9 \pm 1.8 \cdot 10^{-1}$
Tyr128Phe	245 ± 20	46 ± 7	5.3 ± 1.2	6.7 ± 0.7	9.0 ± 2	$7.4 \pm 2.2 \cdot 10^{-1}$

NQO1 Reduction by NADPH

	Fast			Slow		
	k_{HT} (s^{-1})	K_d^{NADPH} (μM)	k_{HT}/K_d^{NADPH} ($s^{-1}\cdot\mu M^{-1}$)	k_{HT} (s^{-1})	K_d^{NADPH} (μM)	k_{HT}/K_d^{NADPH} ($s^{-1}\cdot\mu M^{-1}$)
WT[a]	261 ± 13[d]			7.8 ± 0.3[b]		
Tyr126Ala	40 ± 1	6.3 ± 1.4	6.3 ± 1.4	18.4 ± 0.9	17.2 ± 2.0	1.1 ± 0.1
Tyr128Ala	175 ± 5	35 ± 3	5.0 ± 0.5	21.2 ± 1.8	11.0 ± 2.7	1.9 ± 0.5
Tyr126Glu	$3.2 \pm 0.1 \cdot 10^{-3}$[c]	N.a.[c]	N.a.[c]	$9.2 \pm 2.0 \cdot 10^{-4}$[c]	N.a.[c]	N.a.[c]
Tyr128Glu	$2.5 \pm 0.2 \cdot 10^{-1}$[c]	N.a.[c]	N.a.[c]	$8 \pm 1 \cdot 10^{-2}$[c]	N.a.[c]	N.a.[c]
Tyr126Phe	78 ± 6[d]			3.0 ± 0.5[d]		
Tyr128Phe	169 ± 5[d]			12.5 ± 0.9[d]		

[a]Data from [7,19]; [b]k_{obs} is independent of [NAD(P)H], therefore, data do not allow to determine $K_d^{NAD(P)H}$ (N.a., not applicable) and the given value corresponds to a limiting k_{HT} calculated as the average of k_{obs} at different [NAD(P)H]; [c]k_{obs} is linearly dependent on [NAD(P)H], therefore data do not allow to determine neither $K_d^{NAD(P)H}$ nor k_{HT} (N.a., not applicable) and the given value corresponds to the second-order rate constant of the process calculated as the slope of the k_{obs} vs. [NAD(P)H] plot ($s^{-1}\cdot\mu M^{-1}$); [d]Reaction is too fast and k_{obs} values (particularly for the fast process, since it occurs in part within the instrumental dead time) cannot be accurately determined when increasing the NADPH:NQO1 ratio. The presented values correspond to k_{obs} values determined at stoichiometric concentrations. [Correction added on 10 April 2026 after first online publication: This table has been updated.]

estimation of the dissociation constant ($K_{d,fast}^{NAD(P)H}$) for the NAD(P)H:NQO1 reactive complexes, as well as the limiting HT rate constant ($k_{HT,fast}^{NAD(P)H}$). The Tyr126Ala and Tyr128Ala variants increased slightly the $K_{d,fast}^{NADH}$ values relative to the WT enzyme by 2.1- and 1.3-fold, respectively, while the $k_{HT,fast}^{NADH}$ decreased by ~5.5-fold for both mutants (Table 1). These analyses revealed that the Tyr126Ala and Tyr128Ala variants retained only 10% and 15%, respectively, of the catalytic efficiency exhibited by the WT in the *fast* process for the flavin reductive half-reaction. The effects of these mutations on the *slow* process were milder, with efficiency reduced to 30% and 55% of the WT levels, respectively (Table 1), indicating changes in synchronization between the two active sites and a decrease in the negative cooperativity. The $K_{d,fast}^{NADPH}$ values for Tyr126Ala and Tyr128Ala were 5-fold lower and 1.8-fold higher, respectively, than their corresponding $K_{d,fast}^{NADH}$ values. The $k_{HT,fast}^{NADPH}$ for Tyr126Ala was nearly identical to $k_{HT,fast}^{NADH}$, while in Tyr128Ala it increased by 3.3-fold. As a result, the *fast* process was more efficient with NADPH than with NADH, by 3.7- and 1.7-fold for Tyr126Ala and Tyr128Ala, respectively. Although the effect of these mutations on the *slow* process was less pronounced than those observed for $K_{d,fast}^{NADPH}$ and $k_{HT,fast}^{NADPH}$, both variants exhibited more than a 2-fold increase in efficiency with NADPH compared to NADH. Overall, these results indicate that the Tyr126Ala and Tyr128Ala mutations, despite being non-conservative, retain the specificity toward NADPH. However, they disrupt the functional cooperativity between the two active sites, likely through changes in the native-state conformational ensemble, specifically, the balance between more and less catalytically competent states [6,7].

The Tyr126Glu and Tyr128Glu variants in NQO1 had a strong deleterious impact on the NAD(P)H-dependent flavin reductive half-reaction, at both the *fast* and *slow* processes (Table 1, Figs 10C, D, 11C, D, S11C, S11D, S12C and S12D). Despite nearly full reduction of the FAD was achieved for both variants

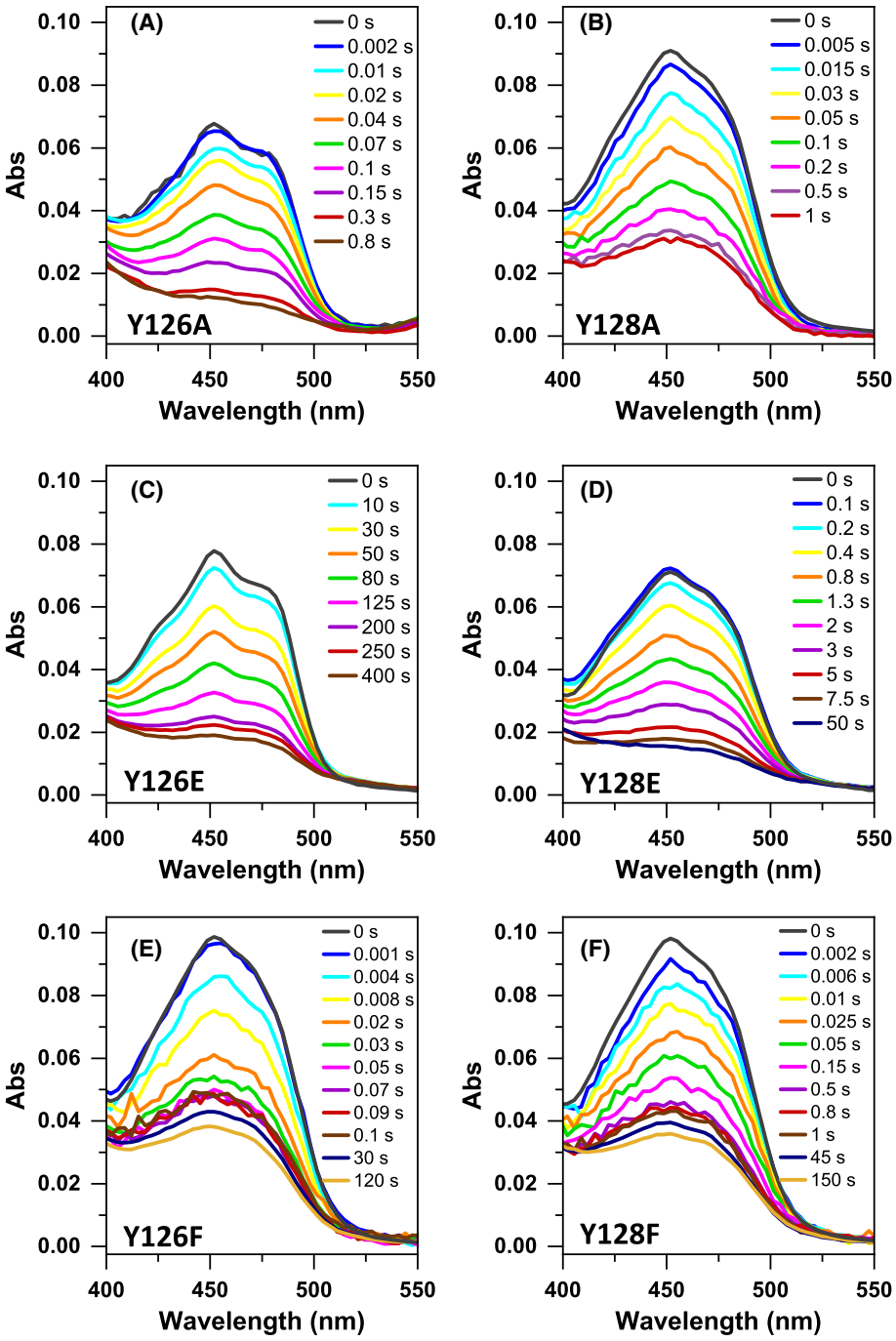

Fig. 10. Time-dependent spectra of the flavin reduction of $NQO1_{ox}$ variants by NADH. Spectral evolution after mixing NQO1 (calculated as protein fully loaded with FAD at the flavin band I: 7.5–9 μM, except for Y126A where the amount of fully holoprotein used is estimated around 6 μM) with NADH (20 μM) in 20 mM HEPES-KOH, pH 7.4, at 6 °C. Panels (A–F) correspond to the indicated variants. Different colored lines show the spectra at different reaction times as indicated in the corresponding legends. The dark gray line represents the spectrum of NQO1 before mixing with NADH. Absorption is shown in AU. Data are representative from $n > 3$.

with both coenzymes, the corresponding values for $k_{obs,fast}$ and $k_{obs,slow}$ were markedly smaller than those observed for the WT under equivalent conditions (Fig. 12A–D and Table 1). Noticeably, in this case, the amplitude of the *fast* process was smaller than that of the *slow* process. These results suggest that the *slow*

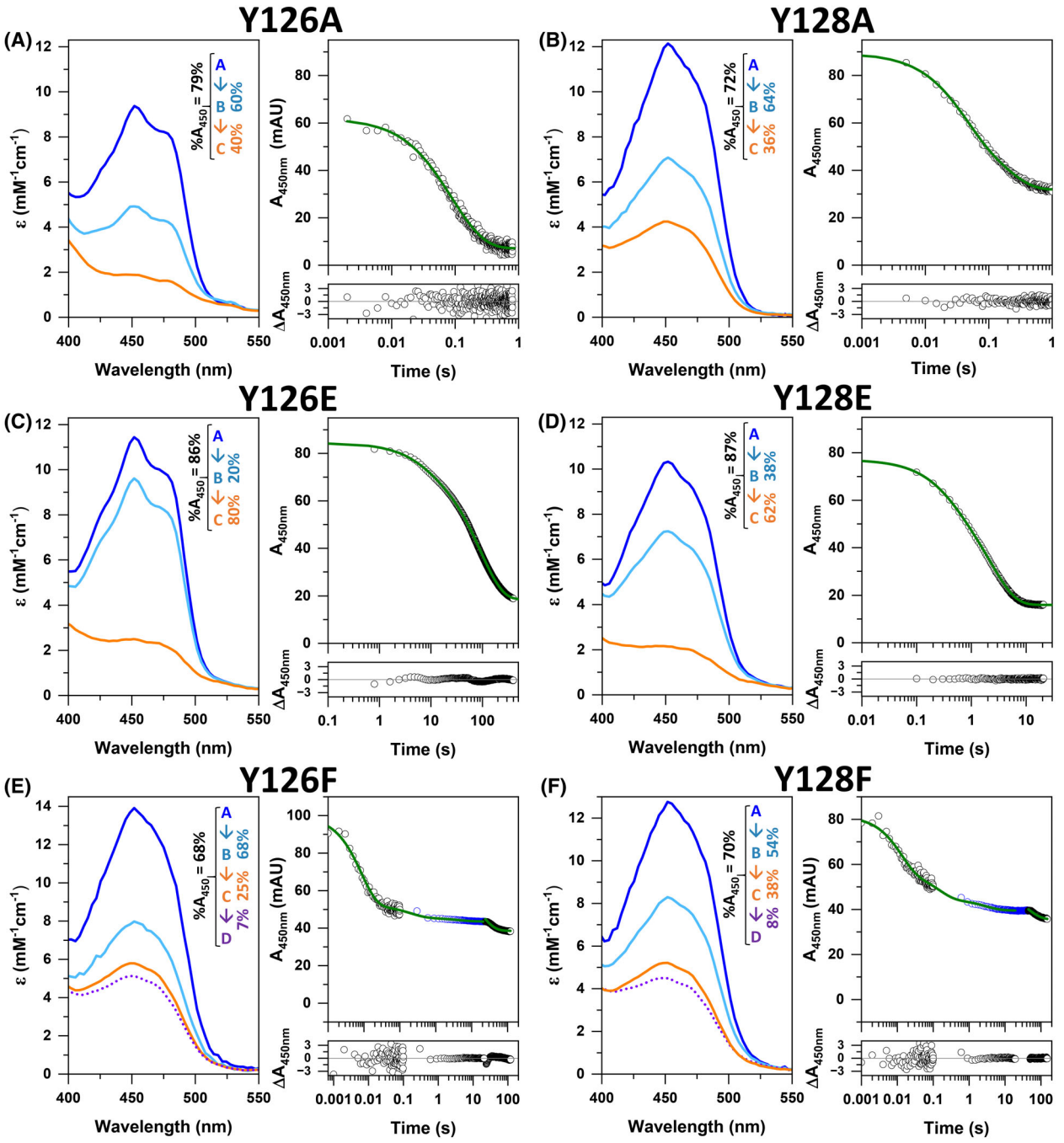

Fig. 11. Evaluation of individual kinetic processes for the flavin reduction of NQO1 variants by NADH. (A–F) show on the left panels the deconvolution into spectral species along the process for the indicated NQO1 variants. The % of the total A_{450} evolved during the entire reaction is indicated, as well as the % of the A_{450nm} for the overall reaction corresponding to the *fast* (A → B, species A is transformed into species B) and *slow* (B → C) processes. In the case of Y126F and Y128F variants, an additional (C → D) process describes a final very slow reaction that is observed separated from the major ones. A-F show on the right panels time evolution for flavin reduction as followed by changes in A_{450nm} (black open circles). Lines are best fits to a two-step model (A → B → C) (green lines). For Y126F and Y128F mutants a lag phase separates these processes from a final very slow process that accounts for a very small amplitude change: in these cases, this process (C → D) has been independently fitted. The lower right panels show the corresponding residuals (black open circles) for data fitting. A_{450nm} and ΔA_{450nm} are shown in mAU. In all cases, shown data correspond to representative transients presented in Fig. 10 after mixing NQO1 with NADH in 20 mM HEPES-KOH, pH 7.4, at 6 °C. Data are representative from $n > 3$.

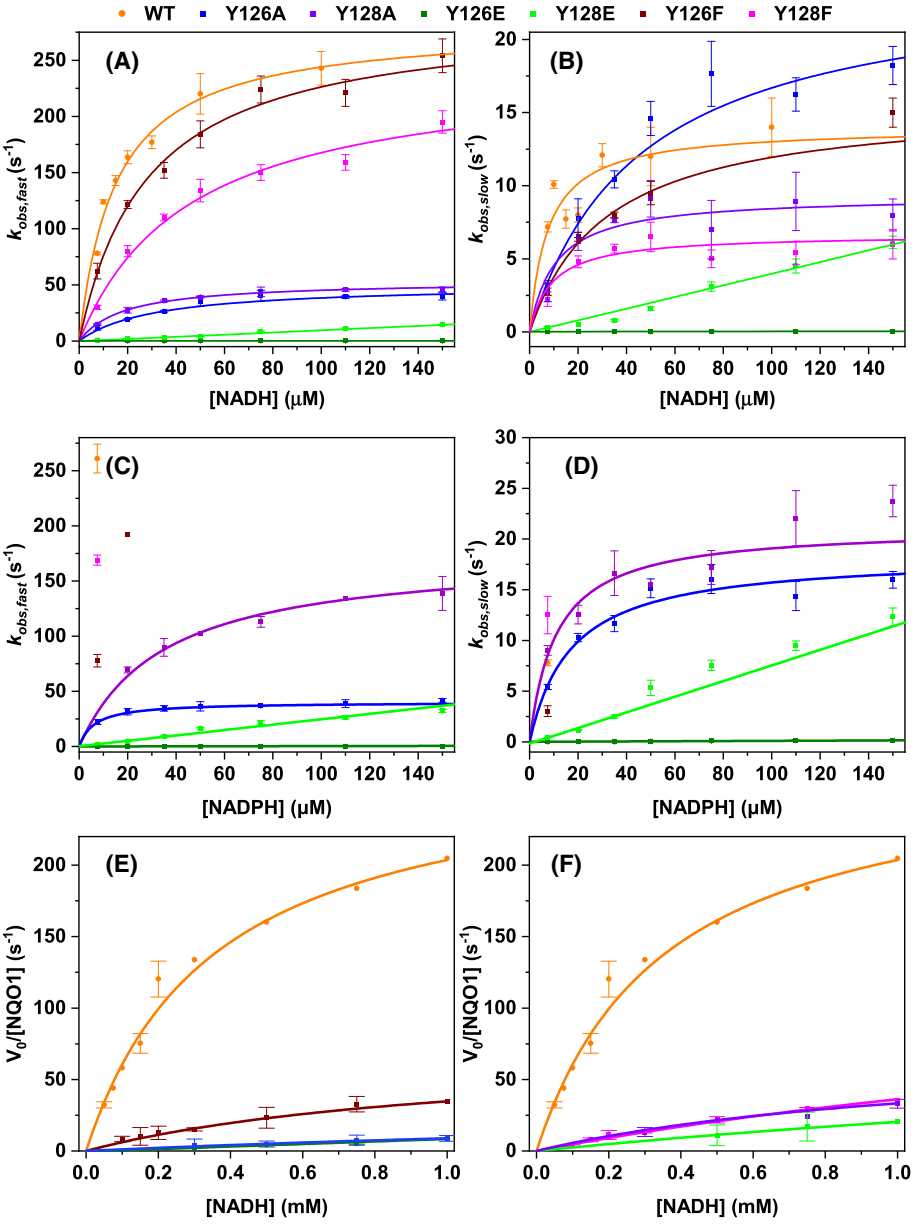

Fig. 12. Effects of Tyr126 and Tyr128 mutations of NQO1 on the kinetic parameters. Dependence of the pre-steady-state observed rate constants for reductive HT for the (A) *fast* and (B) *slow* processes on NADH concentration, and for the (C) *fast* and (D) *slow* processes on NADPH concentration. Steady-state Michaelis–Menten plots for mutants at (E) Tyr126 and (F) Tyr128 when using NADH as hydride donor and DCPIP as acceptor. Experimental data for each mutant are colored by symbols as indicated in the figure code. Lines are best fits to a hyperbolic Michaelis function or to a straight line. Errors are the s.d. from at least three replicates.

pathway predominates over the *fast* one, thereby affecting the functional cooperativity between the two active sites of the enzyme. Moreover, for both *fast* and *slow* processes, the $k_{obs}^{NAD(P)H}$ values of the Tyr128-Glu variant showed a slight linear dependence on the NAD(P)H concentration (allowing estimation of a very slow value for the second-order rate constant). In contrast, the corresponding values for Tyr126Glu showed a linear dependence on NADPH concentration but were essentially independent of NADH concentration (Fig. 12A–D and Table 1). These results further support a remarkable effect on the coenzyme performance when either Tyr126 or Tyr128 are largely perturbed. Noticeably, the k_{obs}^{NADPH} values for both mutants were slightly higher than the corresponding k_{obs}^{NADH} values across the concentration range

evaluated. Altogether, these observations indicate that substitutions with Glu prevent NQO1's ability to either bind the coenzyme or achieve the catalytically competent coenzyme orientation for HT from its nicotinamide to the isoalloxazine of FAD, thus limiting the overall reaction kinetics [19]. These data also suggest that the deleterious effect on HT is more pronounced when substituting Tyr126 as compared with Tyr128.

Remarkably, the conservative variants Tyr126Phe and Tyr128Phe produced NQO1 enzymes in which FAD reduction reached approximately 65–70% across the NAD(P)H concentration ranges evaluated (Table 1, Figs 10E,F, S11E and S11F). Moreover, in both variants, the FAD reduction profiles were best described by two kinetic processes, *fast* and *slow*, with the *fast* phase showing just a slightly larger amplitude (representative analyses are shown in Figs 11E,F, S12E and S12F). It is noteworthy that both mutants displayed a final, slow decrease in the amplitude of flavin band I, independently of the coenzyme. This process occurred after the *fast* and *slow* phases and was characterized by very low k_{obs} values, which were essentially independent of the NAD(P)H concentration. As observed for the WT, $k_{obs,fast}^{NADH}$ and $k_{obs,slow}^{NADH}$ showed hyperbolic dependences on NADH concentration (Fig. 12A,B). However, when using NADPH as a hydride donor, the high $k_{obs,fast}^{NADPH}$ values prevented evaluating the NADPH concentration profile (Fig. 12C). Both variants showed minor effects in $k_{HT,fast}^{NADH}$ values, whereas the $K_{d,fast}^{NADH}$ values increased moderately by ~1.8 and ~3-fold for Tyr126Phe and Tyr128Phe, respectively (Table 1). Consequently, these mutants retained about 55% and 30%, respectively, of the catalytic efficiency exhibited by the WT for the *fast* process of the flavin reductive half-reaction. In the case of the *slow* process, the catalytic efficiency decreased to approximately 30% and 43% of WT levels for Tyr126Phe and Tyr128Phe, respectively.

The NQO1 stopped-flow analysis presented significant challenges due to the substantial differences in reaction rates between *fast* and *slow* processes. This disparity hindered complete data collection during the rapid onset of the *fast* phase, leading to the above amplitude estimations being qualitative rather than quantitative. Initial reports on the WT NQO1 NAD(P)H reductive half-reaction already indicated that a 50:50 amplitude ratio was only achieved in the presence of a potent NQO1 inhibitor that significantly slowed the *fast* phase [7].

Here, it is also worth noting that for certain mutants, as well as for WT, the presented data show near-complete reduction of both FAD cofactors, in agreement with full occupancy of both active sites throughout the measured reaction time. However, Tyr to Glu substitutions resulted in a qualitative decrease in both the rate and amplitude of the *fast* phase, likely due to changes in the structural and dynamic properties of the coenzyme binding cavity that prevent coenzyme access. In contrast, other variants did not achieve full reduction of both FAD cofactors, even though the rates of the *fast* phase were only moderately affected. These findings highlight the critical role of these tyrosine residues in substrate binding and occupancy during the NQO1 catalytic cycle. They also underscore the need for structural investigation to understand how these residues influence the enzyme's conformational dynamics and asymmetric nature.

Given that Phe mutations had only a mild impact on the pre-steady-state flavin reductive half-reaction, we next evaluated the impact of all mutations on NQO1 catalytic turnover during quinone substrate reduction. Under steady-state conditions, WT NQO1 exhibited effective K_m^{NADH} and K_m^{DCPIP} values of 276 ± 9 μM and 6.1 ± 0.9 μM, respectively (Fig. 12E,F and Table 2). The relatively high K_m^{NADH} value compared to the $K_{d,fast}^{NADH}$ derived from the FAD reductive half-reaction highlights the complexity of NQO1 catalysis, as these parameters describe different aspects of enzyme function. While $K_{d,fast}^{NADH}$ reflects the binding affinity of NADH prior to HT to the FAD cofactor, K_m^{NADH} provides insights into the overall efficiency of steady-state turnover, encompassing multiple steps and averaged contributions from both active

Table 2. Steady-state kinetic parameters and midpoint reduction potentials for the NQO1 variants at Tyr126 and Tyr128. Primary kinetic data and fittings are shown in Fig. 12E,F. Potentials were determined by using the Xanthine/XO method in 20 mM HEPES-KOH pH 7.4 at 25 °C with examples for primary data and fittings shown in Fig. S13.

	k_{cat} (s^{-1})	K_m^{NADH} (mM)	k_{cat}/K_m^{NADH} ($s^{-1}\cdot mM^{-1}$)	$E_{ox/hq}$ (mV)
WT	276 ± 9	0.35 ± 0.03	788 ± 32	-125 ± 3
Tyr126Ala	38 ± 19	3.3 ± 2.0	11.5 ± 10	-136 ± 1
Tyr128Ala	98 ± 28	1.4 ± 0.8	70 ± 58	-132 ± 1
Tyr126Glu	8.84 ± 1.2[a]	N.a.[a]	N.a.[a]	-149 ± 1
Tyr128Glu	18.2 ± 1.9[a]	N.a.[a]	N.a.[a]	-128 ± 1
Tyr126Phe	72 ± 7	1.1 ± 0.2	65 ± 17	-133 ± 1
Tyr128Phe	142 ± 30	2.9 ± 0.8	49 ± 23	-138 ± 3

[a]k_{obs} is linearly dependent on [NADH]; therefore, data do not allow us to determine neither K_m^{NADH} nor k_{cat} (N.a., not applicable), and the given value corresponds to the second-order rate constant of the process calculated as the slope of the initial velocity vs. [NADH] plot ($s^{-1}\cdot\mu M^{-1}$).

sites. The evaluation of the Tyr126 and Tyr128 mutations revealed significant alterations in the steady-state parameters. In all mutants, K_m^{NADH} increased and k_{cat} decreased, resulting in a catalytic efficiency below 10% of that of the WT enzyme (Fig. 12E,F and Table 2). Nonetheless, comparison of K_{HT}^{NADH} values with k_{cat} values indicates that only the *fast* process of the flavin reductive half-reaction is catalytically relevant, as observed for WT NQO1. Furthermore, all mutants displayed nearly invariant steady-state rates with respect to DCPIP concentration, which hindered the determination of K_m^{DCPIP}. This suggests that the mutations altered the binding or configuration of the active site, thereby modifying substrate specificity toward quinones and potentially enabling alternative binding or processing modes. Deleterious effects were particularly pronounced for the Glu-substituted mutants, which showed very poor turnover in quinone reduction, consistent with their weak NADH-dependent activity observed in the flavin reductive half-reaction. Mutations to Ala and Phe also caused stronger impairment than in the pre-steady-state reductive kinetics parameters, implying that the observed decrease in their steady-state turnover values may be due to decreases in the rate of another step in the reaction different from NADH reduction. Altogether, these findings suggest that the hydroxyl groups and the side-chains present in the original tyrosine residues are relevant for the competent binding of both substrates—NADH and oxidized quinone—and for the subsequent dissociation of their corresponding products—NAD^+ and reduced quinone.

Mutations at Tyr126 and Tyr128 hardly affect the NQO1 FAD reduction potential

NQO1 reduction was carried out using the non-physiological electron donor xanthine/xanthine oxidase (XO) system, with indigo disulfonic acid as the most suitable two-electron redox dye to equilibrate with the FAD redox couple, as monitored by absorption spectroscopy (Fig. S13A). The dependence of the logarithmic ratio of oxidized to reduced enzyme on that of the dye yielded a slope close to 1, which is consistent with a two-electron transfer process. From this relationship, the midpoint reduction potential ($E_{humanNQO1ox/hq}$) was estimated to be −125 mV (Fig. S13B), with this value being less negative than that of free FAD ($E_{FADox/hq} = -219$ mV, [21]), and also less negative than that reported for the rat NQO1 enzyme ($E_{ratNQO1ox/hq} = -159 \pm 3$ mV) [22]. A similar approach was also used to estimate the midpoint potentials for the Tyr126 and Tyr128 variants (Fig. S13B and Table 2). The mutations had marginal impacts on $E_{humanNQO1ox/hq}$ with values generally between 4 and 15 mV more negative than that of the WT protein. Among them, Tyr126Glu presented the most negative midpoint potential. These observations confirm that the substitutions do not significantly disrupt the intrinsic redox driving force of the reaction but rather interfere with the correct alignment and stabilization of substrates within the active site. Notably, during the determination of these midpoint potentials, additional spectral features appeared within flavin band II, suggesting transient stabilization of an anionic flavin semiquinone intermediate. To verify this, photoreduction and reoxidation experiments were carried out, confirming the formation of an anionic FAD semiquinone upon photoirradiation (Figs S13C and S13D). This intermediate state was not observed during the protein reoxidation by molecular oxygen and is unlikely to occur during the physiological HT events catalyzed by this enzyme *in vivo*.

Mutations at Tyr126 and Tyr128 alter dynamic regions essential for competent and asymmetric substrate binding

Based on the above observations, it was relevant to evaluate the potential impact of these substitutions on the conformation, size, and electrostatic properties of the substrate binding cavity. As shown in Fig. 13, the Tyr126Ala/Glu and Tyr128Ala/Glu mutations significantly influence these structural properties. Furthermore, evaluation of free and ligand-bound active sites in the room temperature structures for WT NQO1 and the NQO1:NAD^+/H complex, considering the four chains within the asymmetric unit, highlights different conformational dynamics for the Tyr126 and Tyr128 side-chains (Fig. 14) [6]. Tyr126, positioned deep within the active site cavity, maintains an almost invariant conformation in both the free and coenzyme-bound states, which is consistent with a role in properly orienting the nicotinamide moiety of the coenzyme toward the isoalloxazine of FAD for catalysis. In contrast, the Tyr128 side-chain exhibits significant conformational variability in both states, showing multiple rotamers in the NADH unoccupied sites in room temperature WT NQO1 and NQO1:NAD^+/H structures (Fig. 14A,B). When NADH is bound, the position of Tyr128 appears correlated to that of the nicotinamide ring (Fig. 14C,D) with Fig. 14D (showing active site 2 of the homodimer made by Chains C and D in the asymmetric unit (ASU)) illustrating a potentially competent pose for HT. These observations further support the above explanation for the differences in HDX

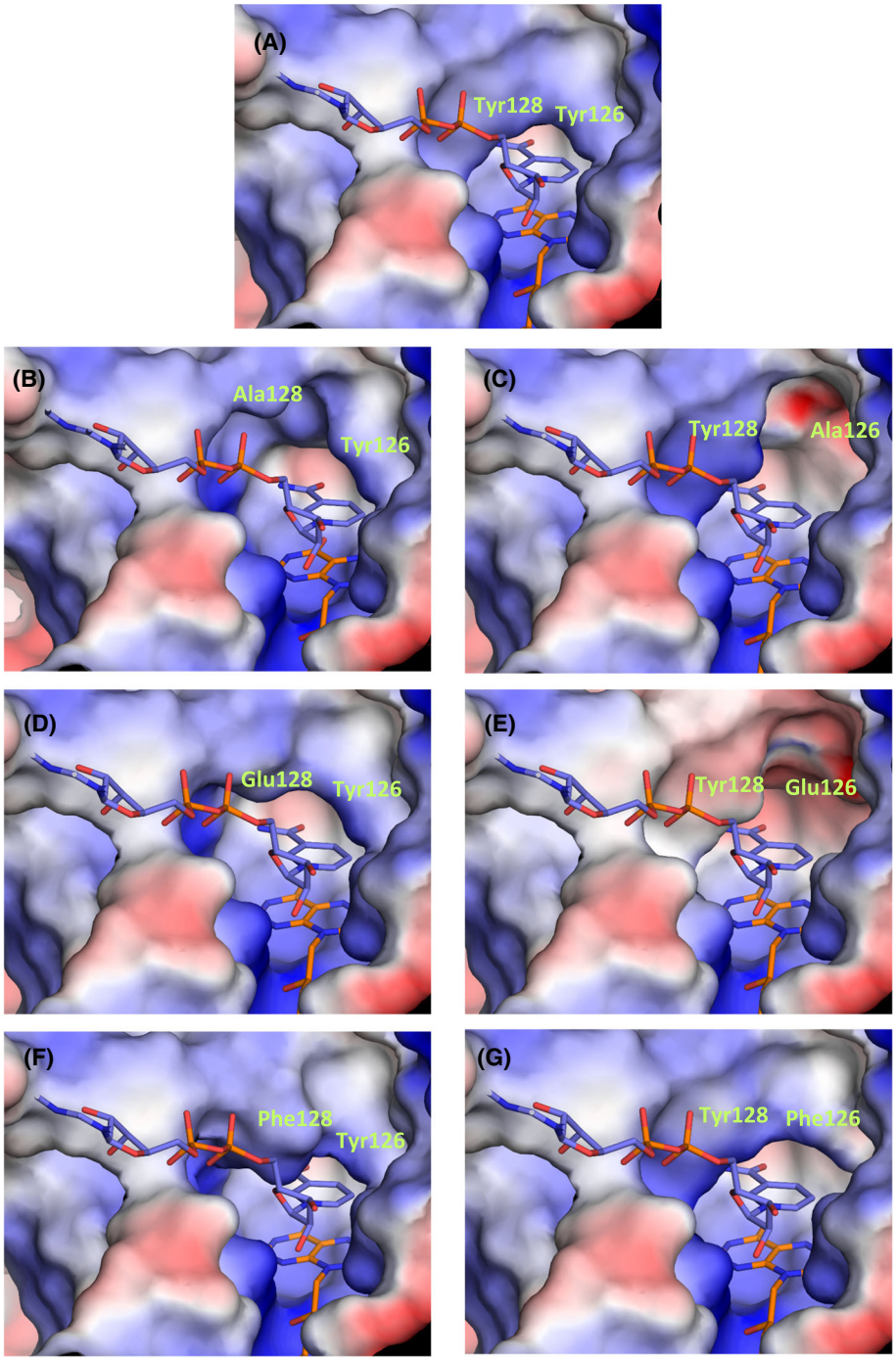

Fig. 13. Predicted effects of Tyr126 and Tyr128 substitutions on the size and electrostatics of the NAD^+/H binding site of NQO1. Electrostatic surface representation of the coenzyme binding site, showing the interaction of NAD^+/H (violet) with key residues forming the nicotinamide binding pocket (surface) and the FAD (orange). (A) Configuration of the coenzyme binding site cavity in the crystal structure of the WT NQO1:NAD^+/H WT complex (PDB 8RFM, chains C and D). (B–G) Structural models of variants with Ala, Glu, and Phe substitutions at positions 126 and 128, illustrating their predicted effects on the cavity size and electrostatic potential. For comparison, positions of FAD and NAD^+/H as observed in the WT structure of the complex are maintained also in mutant models as sticks with carbons in orange and violet, respectively. Structure visualized using PYMOL Software.

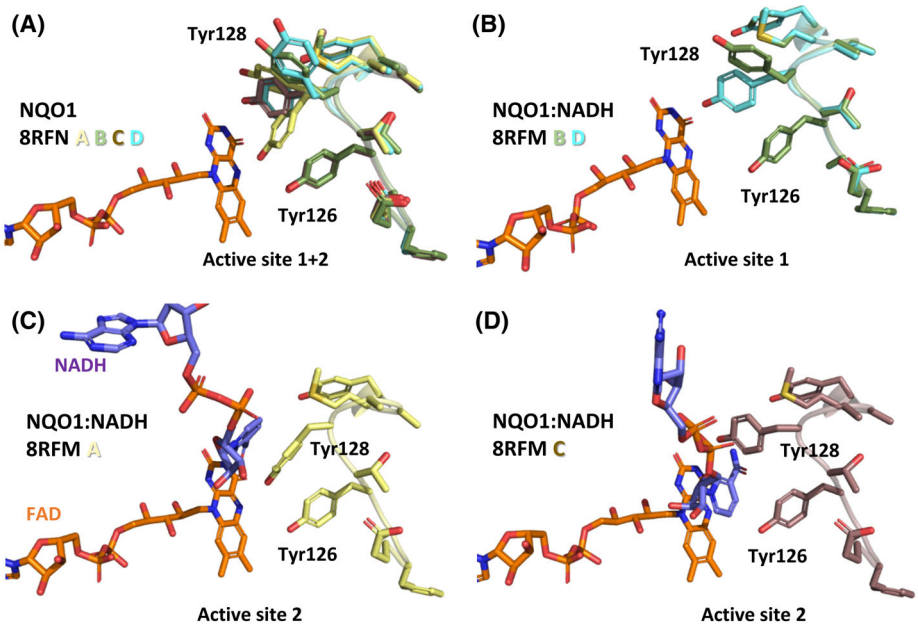

Fig. 14. Rotamer conformations of Tyr126 and Tyr128 in room temperature structures of free NQO1 and the NQO1:NAD^+/H complex. (A) Overlapping of residues 123–132 from the four chains (A-D) in the ASU of free NQO1 (PDB 8RFN). (B) Overlapping of residues 123–132 from the two chains (B and D) corresponding to the NADH-unbound active site 1 in the ASU of the NQO1:NAD^+/H complex (PDB 8RFM). (C,D) Residues 123–132 in chains A (C) and C (D) of the NADH-bound active site 2 in the ASU of the NQO1:NAD^+/H complex (PDB 8RFM). The positions of FAD and NADH (when present) are shown as sticks. Structure visualized using PYMOL Software.

between these closely spaced tyrosine residues. Located at the entrance to the active site, Tyr128 likely plays a dynamic role in facilitating access and exit of the redox-active portion of substrates and products.

The Ala substitutions, particularly Tyr126Ala, are expected to produce noticeable effects on the size of the active site cavity (Fig. 13B,C). Therefore, these mutations would surely introduce additional challenges for the nicotinamide and quinone substrates to adopt the catalytically competent conformations. Overall, the changes induced by these substitutions underscore the critical role of the properties of the substrate binding cavity in enzyme functionality and conformational dynamics. Furthermore, these observations are consistent with the HDX-MS data, which show that NAD^+ has minor local and long-range stabilizing effects on key protein segments, while producing limited thermal stabilization, particularly on the Tyr126Ala mutant (Figs 2, 7 and 9). The enlarged cavity produced by the Ala substitutions may also facilitate greater substrate movement, enabling it to sample multiple conformational ensembles within the binding site. Such enhanced flexibility reduced the population of catalytically competent complexes and increased conformational dynamics, ultimately resulting in decreased HT catalytic efficiency compared to the WT scenario.

Due to the absence of detectable HDX-MS changes upon NAD^+ addition and the drastic loss of catalytic activity in both steady-state and pre-steady-state for both Glu mutants, the most plausible explanation is that NAD^+/H hardly binds to these variants and hence fails to stabilize NQO1. This is also consistent with the structural positions of Tyr126 and Tyr128, where replacement by a negatively charged residue could electrostatically repel NAD(H), preventing the nicotinamide cofactor from residing in the active site cavity. In fact, modeling of a glutamic acid residue at either position 126 or 128 results in a markedly altered cavity geometry, with a wider and less positively charged environment at the substrate binding site, particularly, in the Tyr126Glu variant (Fig. 13D,E). Such alteration is likely to hinder the binding of both NADH and quinone substrates, particularly it may avoid positioning the pyrophosphate moiety of NADH and, therefore, prevent the catalytically competent orientation of the nicotinamide moiety relative to the isoalloxazine ring of FAD. Notably, mutation Tyr128Glu appears to stabilize the protein despite its detrimental effects on catalysis (Figs 3A and 4). This stabilization may result from the introduction of glutamate, which could enhance rigidity in specific regions, and particularly at the entrance of the active site, consequently affecting both the enzyme's conformational dynamics and the

electrostatic properties of the substrate binding site. In fact, the three residues of the Tyr126-Thr127-Tyr128 hub have been shown as phosphorylation sites in human NQO1 (https://www.phosphosite.org/proteinAction.action?id=14721&showAllSites=true) [17,23,24]. If future experiments confirm these predictions, the introduction of negative charges at the coenzyme binding site upon phosphorylation—emulated in the Tyr126Glu and Tyr128Glu variants—could lead to reversible inactivation of the NQO1 function.

Finally, the Phe mutations introduced minimal perturbations across the different protein regions and produced the most similar kinetics to the WT, especially in the pre-steady-state regime, consistent with their similar dynamic response to coenzyme binding. Nonetheless, these substitutions show that the tyrosine residues play an essential role in properly positioning the quinone substrate within the active site for efficient catalysis.

Beyond the specific roles of Tyr126 and Tyr128 within the substrate binding site, this study highlights the identification of dynamic regions that are essential for optimal coenzyme binding, efficient reduction of FAD by NADH, and overall NQO1 catalysis. The intrinsic conformational dynamics of NQO1 act as a structural scaffold that mediates communication between the two active sites upon coenzyme binding (Fig. 7), being influenced by the nature of residues at positions 126 and 128 (Figs 3B and 9). Such observations are also in line with mutations Tyr126Ala/Glu having a higher impact on enzyme conformational dynamics than those at the position of Tyr128, since Tyr126 sits deep in the substrate binding cavity and is a central part of the enzyme active site. Hence, Tyr mutations here studied produce different perturbations of the dynamics of the natural state ensemble, due to the different roles envisaged for each of these two residues during competent allocation of substrates for WT NQO1 catalysis.

Conclusions

In this work, we have experimentally evaluated the roles of Tyr126 and Tyr128 on conformational dynamics, competent allocation of substrates and enzyme catalysis, synchronization of active sites and preference for NADPH *versus* NADH as hydride donors in the human NQO1 homodimeric flavoenzyme [6,7,9,14,18]. We systematically described how large perturbations at these residues lead to substantial drops in catalytic efficiency and changes in the catalytic mechanisms. These changes stem from alterations in both local structural integrity at the substrate binding site and the long-range propagated conformational dynamics that connect the two active sites. In some cases, large perturbations of active site shape and electrostatics may contribute to the effects observed on NQO1 substrate binding (Figs 9 and 12, Table 1). In these contexts, our work provides several essential conclusions. First, the size characteristics of Tyr126 and Tyr128, along with the hydrogen bonding network among their hydroxyls and their aromatic stacking against the reactive moieties of substrates, are key for their orientation in the NQO1 active site during catalysis. Second, development of inhibitors or activators of NQO1 for therapeutic purposes [4,13] must take into consideration the structural and conformational dynamics of these residues and the overall protein ensemble in the NQO1 catalytic cycle and non-synchronization of redox processes at the two active sites. Moreover, it should also be considered the possibility of the two Glu mutants mimicking phosphorylation events. This inactivation may have significant physiological and pathological consequences, adding another layer of complexity in understanding the relationships between genotypic diversity of NQO1 and the propensity to develop disease [8,17,19,25–28]. In addition, our study shows that ligand binding to WT NQO1 causes local conformational stabilization that propagates far beyond the binding site, whereas mutations Tyr126Glu/Ala and Tyr128Ala caused a negative impact on conformational stability that also disseminates far from the mutated sites. The interplay between Tyr126 and Tyr128 and the enzyme's structural dynamics here described also highlights their relevance in preserving optimal NQO1 conformational dynamics for overall activity and efficiency. The present study further confirms the substantial local plasticity of NQO1 in response to perturbations observed in previous studies [6,12,15–17,19], while opening avenues for a better understanding of the molecular bases for long-range dynamic effects propagating between active sites.

Materials and methods

Protein expression and purification

Mutations were introduced by site-directed mutagenesis in the WT NQO1 cDNA cloned into the pET-15b vector (pET-15b-NQO1) by GenScript (Leiden, The Netherlands). Codons were optimized for expression in *Escherichia coli* and mutagenesis was confirmed by sequencing the entire cDNA. The plasmids were transformed into *E. coli* BL21(DE3) cells (Agilent Technologies, Santa Clara, USA) for protein expression. These constructs contained

a N-terminal His_6-tag to ease purification. Expression and purification of NQO1 variants were carried out as described [7,15] using immobilized nickel affinity chromatography columns (Cytiva, Marlborough, USA) and size-exclusion chromatography (Cytiva, Marlborough, USA). Isolated dimeric fractions of NQO1 variants were buffer exchanged to HEPES-KOH buffer 50 mM pH 7.4 using PD-10 columns (Cytiva, Marlborough, USA). The UV–visible spectra of purified NQO1 proteins were registered in a HP8453 UV–Visible spectrophotometer (Agilent Technologies, Santa Clara, USA) and used to quantify the content of FAD as described [7] using protein variants from two different purifications. The total protein concentration was determined spectroscopically by measuring the absorbance at 280 nm. Meanwhile, the total concentration of redox-active species was assessed by analyzing the absorption band I of the flavin cofactor, being this the concentration used when evaluating kinetics.

Thermal denaturation

Thermal denaturation of NQO1 (1 μM) variants in the absence and in the presence of NAD^+ (1 mM) was monitored by following changes in tryptophan emission fluorescence in HEPES-KOH 50 mM at pH 7.4 as described [29]. T_m values were reported as mean ± s.d. of three independent measurements.

Proteolysis

Kinetic proteolysis studies by thermolysin were performed in 50 mM HEPES-KOH, 10 mM $CaCl_2$ at pH 7.4 and 25 °C, as recently described [20,29]. 10–20 μM NQO1 variants as purified were incubated with an excess of 100 μM FAD, and experiments were carried out using a final thermolysin concentration of 0.05–0.8 μM. Proteolysis was triggered by the addition of a concentrated protease stock (x10); samples were withdrawn at different time points and stopped with 25 mM EDTA (Ethylenediaminetetraacetic acid, Merck) at pH 8.0. Samples were denatured with Laemmli's buffer and analyzed by polyacrylamide gel electrophoresis in the presence of SDS (SDS/PAGE) containing 12% acrylamide. Gels were scanned and analyzed using the ImageJ software (https://imagej.nih.gov/). Time-dependent decay of uncleaved NQO1 allowed us to determine first-order rate constants (k_{obs}) from fittings carried out using an exponential function. Second-order rate constants (k_{prot}) were obtained by dividing first-order rate constants by the protease concentration used (Fig. 5H and Table S2). Mutational effects on the local thermodynamic stability of NQO1 variants ($\Delta\Delta G_{prot}$; primary cleavage site at S71-V72) were determined as previously described [8,30].

Hydrogen-deuterium exchange monitored by mass spectrometry (HDX-MS)

Hydrogen-deuterium exchange kinetics were monitored for all NQO1 variants under the FAD and FAD-NAD^+ conditions. Prior to the HDX-MS experiments, all variants were overloaded with a large excess of FAD (typically 1 mM) and subsequently buffer exchanged. Proteins were then pre-incubated for 5 min at 21 °C with 10-molar excess of FAD prior to the exchange. In the case of FAD-NAD^+ conditions, another pre-incubation with 500-molar excess of NAD^+ was done. HDX-MS was carried out at 21 °C using a 10-fold dilution to D_2O-based buffer (50 mM HEPES-KOH, pD 7.4/pH_{read} 7.0) enriched with 5 mM NAD^+ for FAD-NAD^+ conditions. Protein concentration during exchange was 1 μM. Exchange times were 20, 180, 600, 3600, and 10 800 s, and the time points 20, 180, and 3600 s were triplicated yielding an average S.D. of 1.3% D. HDX was quenched by mixing with cooled 1 M glycine-HCl, pH 2.3 at 1:1 ratio. A PAL DHR autosampler (CTC Analytics AG, Zwingen, Switzerland) controlled by Chronos software (AxelSemrau, Sprockhövel, Germany) was used to prepare HDX reactions and subsequent injection onto the LC system comprising a temperature-controlled box and Agilent Infinity II UPLC (Agilent Technologies, Santa Clara, USA) directly coupled to an ESI source of timsTOF Pro mass spectrometer (Bruker Daltonics, Billerica, USA). Here, online proteolysis was done on a mixed bed pepsin/nepenthesin-2 column (bed volume 66 μL) and peptides were captured and desalted on the trap column (SecurityGuard™ ULTRA Cartridge UHPLC Fully Porous Polar C18, 2.1 mm ID, Phenomenex, Torrance, USA) under the flow of 0.4% formic acid (FA) in water driven by the 1260 Infinity II Quaternary pump at the flow rate of 200 $\mu L \cdot min^{-1}$. Peptides were further separated on an analytical column (Luna Omega Polar C18, 1.6 μm, 100 Å, 1.0 · 100 mm, Phenomenex, Torrance, USA) using water–acetonitrile (ACN) gradient (10–45% in 6 min; solvent A: 0.1% FA in water, solvent B: 0.1% FA, 2% water in ACN), which was delivered by the 1290 Infinity II LC pump under the flow rate of 40 $\mu L \cdot min^{-1}$. The LC outlet was directly interfaced ESI source of timsTOF Pro (Bruker Daltonics, Billerica, USA) mass spectrometer operated in the MS mode with a 1 Hz data acquisition. To minimize the loss of deuterium, the LC system was refrigerated to 0 °C. Fully deuterated control samples used for deuterium back-exchange correction were prepared for all variants [31].

Acquired LC–MS data were peak picked and exported in DataAnalysis (v. 5.3, Bruker Daltonics, Billerica, USA) and further analyzed by the DeutEx software (Bruker Daltonics, Billerica, USA) [32]. Data visualization was performed using MSTools (http://peterslab.org/MSTools/index.php) [33]. For peptide identification, the same LC–MS system was used but the mass spectrometer acquired data in data-dependent MS/MS mode using PASEF. The LC–MS/MS data were

searched against a customized database combining sequences of NQO1 (WT, Tyr126Ala/Glu/Phe and Tyr128Ala/-Glu/Phe), common cRAP.fasta (https://www.thegpm.org/crap/) and proteases using MASCOT (v. 2.7, Matrix Science). Search parameters were set as follows: no enzyme, no modifications allowed, precursor tolerance 10 ppm, fragment ion tolerance 0.05 Da, decoy search enabled, FDR < 1%, IonScore > 20 and peptide length > 5. The HDX dataset consisted of 295 peptides providing HDX data. The entire sequence of NQO1 was covered (100% sequence coverage) by peptides of an average peptide length of 11.2 residues and an average redundancy of 12.1. %Dav parameter was calculated as an average of the two time points with maximal absolute differences between compared conditions [15,16,30]. The HDX-MS data have been deposited to the ProteomeXchange Consortium via the PRIDE [34] partner repository with the dataset identifier PXD060224.

Pre-steady-state and steady-state enzyme kinetic analysis

Reductive processes for NQO1 variants upon HT from NAD(P)H were followed under anaerobic conditions using a stopped-flow spectrophotometer (SX.18MV, Applied Photophysics Ltd., Leatherhead, UK) interfaced with a photodiode array detector, essentially as described before [7]. Reactions were performed in 20 mM HEPES-KOH, pH 7.4. The flavin reductive half-reaction was measured by mixing NQO1 variants (7.5 μM) with NAD(P)H ranging from 7.5 to 100 μM. Multiple wavelength absorption data in the flavin absorption region were collected and processed as described [7]. Time-dependent spectral deconvolution was performed by global analysis and numerical integration methods using previously described procedures [7]. Deconvolution was carried out considering two sequential and irreversible processes (A → B → C), which correspond to the two catalytically relevant reactions: A → B (*Fast process*) and B → C (*Slow process*) [7]. This procedure allowed us to determine observed rate constants (k_{obs}) for these steps, as well as spectroscopic properties of A, B, and C species. When observed, hyperbolic dependences of k_{obs} vs. NAD(P)H concentrations were fitted using Eqn (1):

$$k_{obs} = \frac{k_{HT} \cdot [\text{NAD(P)H}]}{K_d^{\text{NAD(P)H}} + [\text{NAD(P)H}]} \quad (1)$$

where k_{HT} is the limiting rate constant for HT and $K_d^{\text{NAD(P)H}}$ is the equilibrium dissociation constant for the coenzyme to a given active site.

Activity measurements of NQO1 variants were carried out in 20 mM HEPES-KOH pH 7.4, using 2,6-dichlorophenolindophenol (DCPIP) as hydride acceptor. Reaction mixtures contained 1 nM of the corresponding NQO1 variant, NADH (0.05–1 mM) and 60 μM DCPIP, or NADH at saturating concentration (1 mM) and variable DCPIP concentration (3–60 μM) [20]. Initial reaction rates were determined from changes in A_{600nm} resulting from the reduction of DCPIP ($\varepsilon_{600nm} = 21\ mM^{-1} \cdot cm^{-1}$). Blanks in the absence of protein were determined and subsequently subtracted from the reaction with NQO1. Kinetic parameters k_{cat} and K_m^{NADH} were determined by fitting initial reaction rates to the Michaelis–Menten equation for those mutants showing hyperbolic dependence.

Estimation of midpoint reduction potentials and photoreduction experiments

Reduction of NQO1 variants by the xanthine/XO method [21,35] was carried out in a closed anaerobic cuvette with a final concentration of ~10 μM of each NQO1 variant, 2 μM benzyl viologen, 500 μM xanthine, 5 μM dye, 10 mM glucose, and 10 $U \cdot mL^{-1}$ glucose oxidase, in 20 mM HEPES-KOH pH 7.4. The indigo disulfonic acid two-electron exchanger ($E_m = -125$ mV, *vs* standard hydrogen electrode) was the dye that better equilibrated with FAD reduction for all variants. After achieving anaerobic conditions, as above indicated using an anaerobic cuvette and a Schlenk line, 4 $\mu g \cdot mL^{-1}$ of bovine milk XO (Sigma-Aldrich) were added from the side arm to the mixture, and spectra were recorded every 2 min scanning from 300 to 750 nm at 25 °C, in a CARY 3500 spectrophotometer (Agilent Technologies, Santa Clara, USA). To ensure thorough equilibration of the components during the experiment, the concentration of XO was set at 15 nM (within the recommended range of 1–100 nM, replicates with 50 nM were also performed, providing the same values and therefore confirming equilibrium was reached) allowing the reductive process to proceed over a period of 2–3 h. Absorption changes accompanying reduction of the indicator dye and the flavoprotein at each point during the xanthine/XO reduction were used to determine the NQO1 $E_{ox/hq}$ value using the Nernst equation as previously reported [21,35]. In short, E are the potentials of the flavin-containing protein (P) and dye (D) as determined by their corresponding Nernst equations (Eqn 2):

$$\begin{aligned} E_P &= E_{m,P} + \frac{2.3RT}{nF} log\left(\frac{[P_{ox}]}{[P_{rd}]}\right) \\ E_D &= E_{m,D} + \frac{2.3RT}{nF} log\left(\frac{[D_{ox}]}{[D_{rd}]}\right) \end{aligned} \quad (2)$$

Slow rates of electron input by XO ensured reaching the equilibrium of oxidized and reduced forms at any given time point of the process. Thus, the NQO1 and dye electrochemical potentials were assumed to be equal, and defining "x" and "y" as the Nernst concentration terms for the NQO1 and dye, respectively (Eqn 3):

$$E_{m,P} + x = E_{m,D} + y \quad (3)$$

When the protein is in redox equilibrium $[P_{ox}] = [P_{rd}]$, "$x = 0$" and "y" can be defined as ΔE, the difference in midpoint potentials of NQO1 and the dye (Eqn 4).

$$E_{m,P} = E_{m,D} + \Delta E \quad (4)$$

Thus, the difference in E_m potential of NQO1 and the dye was calculated from a plot where the log([oxidized]/[reduced] ratio) for sample and dye of each spectrum is plotted against each other. In this particular case, the absorbance changes accompanying reduction of the indicator dye at 610 nm (where the NQO1 does not absorb) and of the flavoprotein at 468 nm (where the indicator has an isosbestic point) at each time point during the xanthine/XO reduction were used to calculate oxidized/reduced ratios for both the protein and the dye (Eqn 5).

$$\frac{[\text{oxidized}]}{[\text{reduced}]} = \frac{A - A_{min}}{A_{max} - A} \quad (5)$$

where A is the observed absorbance with a given time point in the titration, and A_{max} and A_{min} are the maximal and minimal absorbances observed. Plotting such "x" and "y" values on a graph and fitting them to Eqn (4) provides as intercept ΔE, the shift in midpoint potential between the FAD of the NQO1 variant and the dye.

Since experiments with WT NQO1 envisaged transient potential stabilization of its anionic semiquinone, we also evaluated this feature by NQO1 (20 μM) in 20 mM HEPES-KOH pH 7.4, EDTA (3 mM), 5-deazariboflavin (4 μM 5-dRf), glucose (5 mM), and glucose oxidase (10 $U \cdot ml^{-1}$) in a closed anaerobic cuvette. The WT NQO1 sample was stepwise photo-irradiated for 5 s periods with a blue LED strip tube that provides an intensity of 900 μmol photons/($m^2 \cdot s$) around the cuvette. Photoreduction was followed by recording the visible spectra after each irradiation by using a CARY 3500 spectrophotometer (Agilent Technologies, Santa Clara, USA).

Structural modeling

The crystal structure of NQO1 in complex with NAD^+/H (PDB ID: 8RFM, [6]) served as the structural model for generating the figures in this study. Mutations at tyrosine residues 126 and 128 were introduced and their best rotamer optimized using COOT (DOI: [36]), and the modified structures were saved as new PDB files. Structural figures and hydrogen bond interactions were analyzed and visualized using Pymol 3.0.4 (The Pymol Molecular Graphics System, version 3.0.4, Schrödinger, LLC, https://www.pymol.org/).

Author contributions

PM, ALP, and MM conceived the study and planned experiments; MR, JLP-G, PV and DSL performed experiments; DSL, IQ, JMM-G and MM produced structural models and figures; MR, PV, DSL, PM, ALP and MM analyzed data; PM, ALP, and MM contributed reagents or other essential material; ALP and MM drafted the initial version of the paper. All authors read and approved the final version of this manuscript.

Acknowledgements

All authors sincerely acknowledge the significant contributions of Dr. Ángel L. Pey to NQO1 research. Dr. Pey, who passed away prior to the publication of this article, provided invaluable input, insights and dedication that were essential to this research. A.L.P. was founded by the Spanish State Research Agency (Grant number RTI2018-096246-B-I00), Consejería de Economía, Conocimiento, Empresas y Universidad, Junta de Andalucía (Grant number P18-RT-2413), and ERDF/Counseling of Economic transformation, Industry, Knowledge and Universities (Grant B-BIO-84-UGR20). M.M. acknowledges funding from the Spanish State Research Agency and FEDER (MCIN/AEI-FEDER, Grant number PID2022-136369NB-I00) and the Government of Aragón-FEDER (Grant number E35_23R). J.M.M-G. acknowledges the European Union Next Generation EU/PRTR (Grant number CNS2022-135713) and the Spanish State Research Agency (Grant number PID2023-151100NB-I00). P.M. acknowledges support from the MEYS project OP JAK INTER-MICRO (CZ.02.01.01/00/22_008/0004597). Access to the Instruct-CZ center (BioCeV), was supported by CIISB (LM2023042 and CZ.02.01.01/00/23_015/0008175) and Instruct-ERIC Internship to J.L.P-G. (APPID 2545). We also acknowledge Servicios Generales de Apoyo a la Investigación-SAI, Universidad de Zaragoza, for support.

Conflicts of interest

The authors declare no conflicts of interest.

Data availability statement

The mass spectrometry proteomics data that support the findings of this study have been deposited to the ProteomeXchange Consortium (http://proteomecentral.proteomexchange.org) via the PRIDE partner repository with the dataset identifier [PXD060224] and link https://www.ebi.ac.uk/pride/archive/projects/PXD060224. Rest of the data that support the findings of this study are available in Tables 1 and 2, Figs 2–12 and the supporting information of this article.

References

1 Salido E, Timson DJ, Betancor-Fernández I, Palomino-Morales R, Anoz-Carbonell E, Pacheco-García JL, Medina M & Pey AL (2022) Targeting HIF-1α function in cancer through the chaperone action of NQO1: implications of genetic diversity of NQO1. *J Pers Med* **12**, 747.

2 Ross D & Siegel D (2021) The diverse functionality of NQO1 and its roles in redox control. *Redox Biol* **41**, 101950.

3 Asher G, Tsvetkov P, Kahana C & Shaul Y (2005) A mechanism of ubiquitin-independent proteasomal degradation of the tumor suppressors p53 and p73. *Genes Dev* **19**, 316–321.

4 Beaver SK, Mesa-Torres N, Pey AL & Timson DJ (2019) NQO1: a target for the treatment of cancer and neurological diseases, and a model to understand loss of function disease mechanisms. *Biochim Biophys Acta, Proteins Proteomics* **1867**, 663–676.

5 Asher G, Dym O, Tsvetkov P, Adler J & Shaul Y (2006) The crystal structure of NAD(P)H quinone oxidoreductase 1 in complex with its potent inhibitor dicoumarol. *Biochemistry* **45**, 6372–6378.

6 Grieco A, Boneta S, Gavira JA, Pey AL, Basu S, Orlans J, de Sanctis D, Medina M & Martin-Garcia JM (2024) Structural dynamics and functional cooperativity of human NQO1 by ambient temperature serial crystallography and simulations. *Protein Sci* **33**, e4957.

7 Anoz-Carbonell E, Timson DJ, Pey AL & Medina M (2020) The catalytic cycle of the antioxidant and cancer-associated human NQO1 enzyme: hydride transfer, conformational dynamics and functional cooperativity. *Antioxidants* **9**, 1–22.

8 Pacheco-Garcia JL, Anoz-Carbonell E, Vankova P, Kannan A, Palomino-Morales R, Mesa-Torres N, Salido E, Man P, Medina M, Naganathan AN *et al.* (2021) Structural basis of the pleiotropic and specific phenotypic consequences of missense mutations in the multifunctional NAD(P)H:quinone oxidoreductase 1 and their pharmacological rescue. *Redox Biol* **46**, 102112.

9 Megarity CF, Abdel-Aal Bettley H, Caraher MC, Scott KA, Whitehead RC, Jowitt TA, Gutierrez A, Bryce RA, Nolan KA, Stratford IJ *et al.* (2019) Negative cooperativity in NAD(P)H quinone oxidoreductase 1 (NQO1). *Chembiochem* **20**, 2841–2849.

10 Clavería-Gimeno R, Velazquez-Campoy A & Pey AL (2017) Thermodynamics of cooperative binding of FAD to human NQO1: implications to understanding cofactor-dependent function and stability of the flavoproteome. *Arch Biochem Biophys* **636**, 17–27.

11 Pey AL, Megarity CF & Timson DJ (2014) FAD binding overcomes defects in activity and stability displayed by cancer-associated variants of human NQO1. *Biochim Biophys Acta Mol basis Dis* **1842**, 2163–2173.

12 Medina-Carmona E, Rizzuti B, Martín-Escolano R, Pacheco-García JL, Mesa-Torres N, Neira JL, Guzzi R & Pey AL (2019) Phosphorylation compromises FAD binding and intracellular stability of wild-type and cancer-associated NQO1: insights into flavo-proteome stability. *Int J Biol Macromol* **125**, 1275–1288.

13 Betancor-Fernández I, Timson DJ, Salido E & Pey AL (2018) "Natural (and unnatural) small molecules as pharmacological chaperones and inhibitors in cancer."

14 Islam F, Basilone N, Yoo V, Ball E & Shilton B (2024) Evolutionary analysis of quinone reductases 1 and 2 suggests that NQO2 evolved to function as a pseudoenzyme. *Protein Sci* **33**, e5234.

15 Vankova P, Salido E, Timson DJ, Man P & Pey AL (2019) A dynamic Core in human NQO1 controls the functional and stability effects of ligand binding and their communication across the enzyme dimer. *Biomolecules* **9**, 728.

16 Pacheco-Garcia JL, Loginov DS, Anoz-Carbonell E, Vankova P, Palomino-Morales R, Salido E, Man P, Medina M, Naganathan AN & Pey AL (2022) Allosteric communication in the multifunctional and redox NQO1 protein studied by cavity-making mutations. *Antioxidants* **11**, 1110.

17 Pacheco-Garcia JL, Anoz-Carbonell E, Loginov DS, Vankova P, Salido E, Man P, Medina M, Palomino-Morales R & Pey AL (2022) Different phenotypic outcome due to site-specific phosphorylation in the cancer-associated NQO1 enzyme studied by phosphomimetic mutations. *Arch Biochem Biophys* **729**, 109392.

18 Megarity CF & Timson DJ (2019) Cancer-associated variants of human NQO1: impacts on inhibitor binding and cooperativity. *Biosci Rep* **39**, BSR20191874.

19 Pacheco-García JL, Anoz-Carbonell E, Loginov DS, Kavan D, Salido E, Man P, Medina M & Pey AL (2023) Counterintuitive structural and functional effects due to naturally occurring mutations targeting the active site of the disease-associated NQO1 enzyme. *FEBS J* **290**, 1855–1873.

20 Medina-Carmona E, Palomino-Morales RJ, Fuchs JE, Padín-Gonzalez E, Mesa-Torres N, Salido E, Timson DJ & Pey AL (2016) Erratum: conformational dynamics is key to understanding loss-of-function of NQO1 cancer-associated polymorphisms and its correction by pharmacological ligands. *Sci Rep* **6**, 20331.

21 Maklashina E & Cecchini G (2020) Determination of flavin potential in proteins by xanthine/xanthine oxidase method. *Bio Protoc* **10**, e3571.

22 Tedeschi G, Chen S & Massey V (1995) DT-diaphorase. Redox potential, steady-state, and rapid reaction studies. *J Biol Chem* **270**, 1198–1204.

23 Hornbeck PV, Zhang B, Murray B, Kornhauser JM, Latham V & Skrzypek E (2015) PhosphoSitePlus, 2014: mutations, PTMs and recalibrations. *Nucleic Acids Res* **43**, D512–D520.
24 Luo S, Kang SS, Wang Z-H, Liu X, Day JX, Wu Z, Peng J, Xiang D, Springer W & Ye K (2019) Akt phosphorylates NQO1 and triggers its degradation, abolishing its antioxidative activities in Parkinson's disease. *J Neurosci* **39**, 7291–7305.
25 Pacheco-García JL, Cano-Muñoz M, Sánchez-Ramos I, Salido E & Pey AL (2020) Naturally-occurring rare mutations cause mild to catastrophic effects in the multifunctional and cancer-associated NQO1 protein. *J Pers Med* **10**, 207.
26 Pacheco-Garcia JL, Cagiada M, Tienne-Matos K, Salido E, Lindorff-Larsen K & L. Pey A (2022) Effect of naturally-occurring mutations on the stability and function of cancer-associated NQO1: comparison of experiments and computation. *Front Mol Biosci* **9**, 1063620.
27 Lienhart W-D, Gudipati V, Uhl MK, Binter A, Pulido SA, Saf R, Zangger K, Gruber K & Macheroux P (2014) Collapse of the native structure caused by a single amino acid exchange in human NAD(P)H: quinone oxidoreductase(1.). *FEBS J* **281**, 4691–4704.
28 Lienhart W-D, Strandback E, Gudipati V, Koch K, Binter A, Uhl MK, Rantasa DM, Bourgeois B, Madl T, Zangger K *et al.* (2017) Catalytic competence, structure and stability of the cancer-associated R139W variant of the human NAD(P)H:quinone oxidoreductase 1 (NQO1). *FEBS J* **284**, 1233–1245.
29 Medina-Carmona E, Fuchs JE, Gavira JA, Mesa-Torres N, Neira JL, Salido E, Palomino-Morales R, Burgos M, Timson DJ & Pey AL (2017) Enhanced vulnerability of human proteins towards disease-associated inactivation through divergent evolution. *Hum Mol Genet* **26**, 3531.
30 Pacheco-Garcia JL, Loginov D, Rizzuti B, Vankova P, Neira JL, Kavan D, Mesa-Torres N, Guzzi R, Man P & Pey AL (2022) A single evolutionarily divergent mutation determines the different FAD-binding affinities of human and rat NQO1 due to site-specific phosphorylation. *FEBS Lett* **596**, 29–41.
31 Vankova P, Pacheco-Garcia JL, Loginov DS, Gómez-Mulas A, Kádek A, Martín-Garcia JM, Salido E, Man P & Pey AL (2024) Insights into the pathogenesis of primary hyperoxaluria type I from the structural dynamics of alanine:glyoxylate aminotransferase variants. *FEBS Lett* **598**, 485–499.
32 Trcka F, Durech M, Vankova P, Chmelik J, Martinkova V, Hausner J, Kadek A, Marcoux J, Klumpler T, Vojtesek B *et al.* (2019) Human stress-inducible Hsp70 has a high propensity to form ATP-dependent antiparallel dimers that are differentially regulated by cochaperone binding. *Mol Cell Proteomics* **18**, 320–337.
33 Kavan D & Man P (2011) MSTools—web based application for visualization and presentation of HXMS data. *Int J Mass Spectrom* **302**, 53–58.
34 Perez-Riverol Y, Bai J, Bandla C, García-Seisdedos D, Hewapathirana S, Kamatchinathan S, Kundu DJ, Prakash A, Frericks-Zipper A, Eisenacher M *et al.* (2022) The PRIDE database resources in 2022: a hub for mass spectrometry-based proteomics evidences. *Nucleic Acids Res* **50**, D543–D552.
35 Christgen SL, Becker SM & Becker DF (2019) Methods for determining the reduction potentials of flavin enzymes. *Methods Enzymol* **620**, 1–25.
36 Emsley P, Lohkamp B, Scott WG & Cowtan K (2010) Features and development of *Coot*. *Acta Crystallogr D Biol Crystallogr* **66**, 486–501.

Supporting information

Additional supporting information may be found online in the Supporting Information section at the end of the article.

Fig. S1. Structural arrangement of mutations at positions 126 and 128 of NQO1 in relation to the FAD cofactor and the NADH coenzyme.

Fig. S2. SDS/PAGE analysis of purified NQO1 variants.

Fig. S3. UV–visible spectra of purified NQO1 variants.

Fig. S4. HDX-MS of WT NQO1 in the absence or the presence of an excess of NAD^+ (red symbols) for segments comprising residues 1–42.

Fig. S5. HDX-MS of WT NQO1 in the absence or the presence of an excess of NAD^+ for segments comprising residues 43–97.

Fig. S6. HDX-MS of WT NQO1 in the absence or the presence of an excess of NAD^+ for segments comprising residues 98–164.

Fig. S7. HDX-MS of WT NQO1 in the absence or the presence of an excess of NAD^+ for segments comprising residues 165–211.

Fig. S8. HDX-MS of WT NQO1 in the absence or the presence of an excess of NAD^+ for segments comprising residues 212–273.

Fig. S9. SDS/PAGE analysis of NQO1 variants degraded by thermolysin.

Fig. S10. Effect of NAD^+ on the HDX-MS of the different NQO1 variants.

Fig. S11. Time-dependent spectra of the flavin reduction of $NQO1_{ox}$ variants by NADPH.

Fig. S12. Evaluation of individual kinetic processes for the flavin reduction of NQO1 variants by NADPH.

Fig. S13. Midpoint reduction potential of NQO1 variants.
Table S1. Best-fit parameters for the HDX-MS of WT NQO1 in the absence or presence of NAD^+.
Table S2. Second-order rate constants for proteolysis by thermolysin of NQO1 variants.
Table S3. Calculated $\%D_{av}$ for mutants in position 126.
Table S4. Calculated $\%D_{av}$ for mutants in position 128.